ACS Catalysis

pubs.acs.org/acscatalysis

Perspective

Design and Characterization of ALD-Based Overcoats for Supported Metal Nanoparticle Catalysts

Erik Sarnello, Zheng Lu, Soenke Seifert, Randall E. Winans, and Tao Li*

Cite This: *ACS Catal.* 2021, 11, 2605−2619

Read Online

ACCESS | Metrics & More | Article Recommendations | Supporting Information

ABSTRACT: Supported metal nanoparticle (SMN) catalysts are enormously crucial for many catalytic applications. However, catalyst deactivation, caused by sintering and coke formation, is a ubiquitous problem that significantly undermines catalytic processing economics. The application of material overcoating onto supported metal nanoparticles by atomic layer deposition (ALD) offers the solution to inhibit catalyst deactivation. Herein, we discuss examples in which ALD has been used to stabilize SMN catalysts in gaseous and aqueous-phase reactions. We highlight the ALD tools and methods in coating high-surface-area catalysts. Besides, various techniques are introduced to understand better how to characterize the overcoating layer and the catalyst itself. Finally, the outlook for new techniques to characterize the ALD overcoated catalytic materials is discussed.

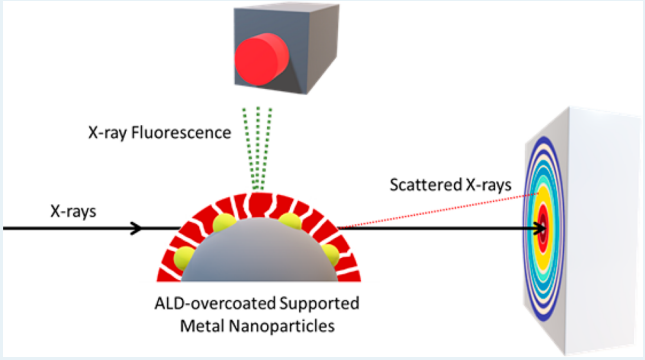

KEYWORDS: *ALD, overcoat, catalyst, porous, SAXS, XAS*

1. INTRODUCTION

Supported metal nanoparticle (SMN) catalysts have become increasingly useful for various catalytic applications, including biomass conversion, CO_2/CH_4 conversion, lithium-ion batteries, and industrial organic reactions.[1−3] SMN catalysts consist of metal nanoparticles deposited on high-surface-area solid support material such as metal oxides or metal−organic frameworks (MOFs). The design versatility of SMN catalysts allows for a variety of different metal catalysts and support materials, which makes them useful for such a broad range of applications. Traditionally, noble metals (Pt, Rh, Ru, and Pd) are used because of their catalytic activity and stability. Noble metals, however, are notoriously expensive because of low availability.[4−6] In the search for more readily available and cheaper catalysts, transition metals such as Co, Ni, Fe, and Cu began to be used in SMN catalyst systems.[5−14] The main drawback of these materials is their susceptibility to catalyst deactivation caused by sintering and coke formation.[15−17] Sintering, which is the fusion of small metal particles in larger aggregates, typically occurs at high temperatures (>500 °C) during operation or catalyst regeneration. The main side effect of sintering is a drastic loss of catalyst surface area resulting in a loss in activity. Coke formation causes catalyst deactivation due to carbon accumulating and blocking the surface of the metal catalyst during operation.[18−20] Catalyst replacement and process downtime due to deactivation results in billions of dollars lost to industry each year.[15] Much research has looked at methods to stabilize SMN catalysts, including the use of core−shell structures, sol−gel coating/coprecipitation techniques, and metal−support interactions to protect against catalyst deactivation.[21−24] Recently, overcoating techniques have shown much promise in protecting metal nanoparticles against sintering. However, some methods can result in overly thick or uneven coatings leading to the loss of catalytic activity.[7,15,18,25,26]

To maintain the efficiency of SMN catalysts, the application of a chemical overcoating requires high precision. Coating techniques such as chemical vapor deposition (CVD) and physical vapor deposition (PVD) suffer from poor reproducibility and uniformity. For example, during a typical CVD process, a substrate is exposed to volatile precursors which react on the substrate surface to create the deposited material.[27] PVD also has inherent disadvantages as it requires "line-of-sight" for deposition. In contrast, layered deposition techniques such as atomic layer deposition (ALD) and molecular layer deposition (MLD) offer total conformal deposition with atomic layer control because of the mechanism's self-limiting nature. The self-limiting, sequential surface reactions follow an A−B binary reaction sequence

Received: November 20, 2020
Revised: February 3, 2021
Published: February 11, 2021

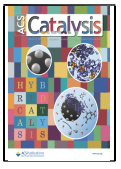

https://dx.doi.org/10.1021/acscatal.0c05099
ACS Catal. 2021, 11, 2605−2619

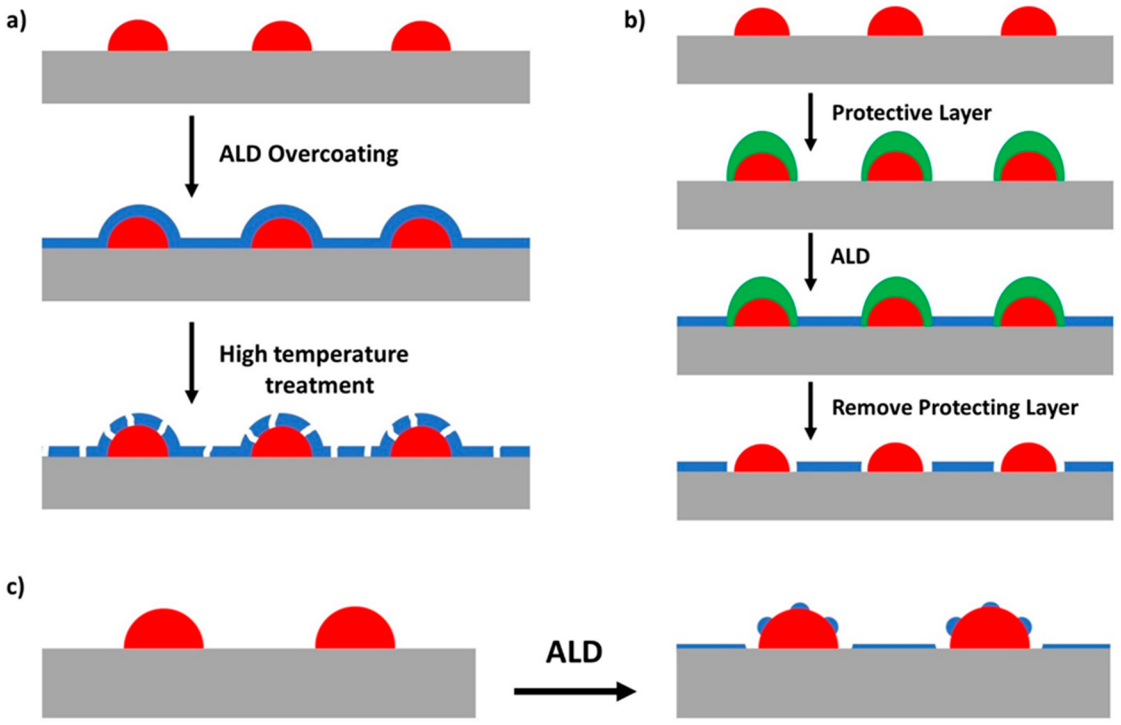

Figure 1. Modification techniques for applying an ALD overcoating to SMNs where gray color represents a support material, green represents the protective layer, blue represents the ALD overcoating, and red represents a metal nanoparticle. Illustrative representation of the following: (a) A continuous thin film is deposited followed by high-temperature heating to induce overcoating densification results in nanosized pores' formation. (b) A protective layer that blocks the ALD materials' deposition is coated on metal nanoparticles followed by ALD and removing the protective layer. (c) Represents selective ALD overcoating as the results of few ALD cycles (typically 1−10 cycles).

during ALD.[28−31] Precursors and reactants are saturated in the reaction chamber to ensure all surface sites undergo the desired reactions. These features lead to extremely uniform and conformal deposition on the substrate with atomic-level thickness control. As a brief example, consider Al_2O_3 ALD, which is usually performed using trimethylaluminum (TMA) and H_2O. In the first step, TMA is pulsed into the reaction chamber and reacts with a surface hydroxyl until all sites are consumed. Second, the chamber is purged to expel the excess TMA with the byproduct methane. Third, water vapor is pulsed into the chamber and reacts with methyl groups on the AlO_x, which forms a hydroxyl group. Lastly, the byproduct methane and excess H_2O is purged from the chamber. These four steps comprise one cycle of Al_2O_3 ALD and result in a growth rate of around 1.2 Å per cycle at 200 °C.[32] The surface chemistry of Al_2O_3 ALD is shown in eqs 1 and 2, where the asterisk indicates the surface species and "(g)" signifies species in gas phases.

$$-OH^* + Al(CH_3)_3(g) \rightarrow -OAl(CH_3)_2^* + CH_4(g) \quad (1)$$

$$-OAl(CH_3)_2^* + 2H_2O(g) \rightarrow -OAl(OH)_2^* + 2CH_4(g) \quad (2)$$

To date, there have been multiple in-depth reviews regarding ALD,[32,33] MLD,[34,35] and their use for the stabilization of catalyst materials.[36−39] This Perspective will focus on the development and advanced characterization methods of ALD overcoated catalysts. We will also discuss the many characteristics for optimal overcoating such as the overcoating thickness, deposition method, and overcoating material.

2. ALD OVERCOATED CATALYST

For applying the overcoating onto SMN catalysts, three general routes have been described. As seen in Figure 1a, the first method involves the overcoating layer's deposition, typically less than 10 nm, which is then calcined before catalyst use.[5,40−43] The high temperatures during the calcination process results in the formation of nanopores in the overcoating layer. The overcoating pores allow access to the catalytic sites while also inhibiting coke formation and sintering.[25,44,45] For the second route (Figure 1b), a chemical protective layer, which inhibits or blocks ALD growth, is first applied to cover the active catalyst phase or metal nanoparticles. A thin film is then deposited via ALD on all areas without the protective layer. The protective layer is then removed by oxidation or other means, thereby leaving the active site or metal nanoparticles exposed while the surrounding overcoating protects the site from deactivation. The final route involves the deposition of an ultrathin, discontinuous coating, as shown in Figure 1c. This can be achieved because, during initial ALD cycles, deposition can occur selectively on metal edge sites or facets.[46−48] By stopping the ALD process after only a few cycles (typically less than 5), the result is the formation of a discontinuous porous coating. The ultrathin coating protects the catalyst nanoparticles from deactivation while still allowing access to the catalytic sites.[49,50] The thickness of the coating layer is a significant factor as an overly thin coating layer may fail to prevent sintering, while a coating that is too thick may inhibit access to catalytic sites and reduce catalytic activity. There is, however, no set standard for an overcoating thickness, which has shown to be highly dependent on the type of catalyst, type of overcoating

https://dx.doi.org/10.1021/acscatal.0c05099
ACS Catal. 2021, 11, 2605−2619

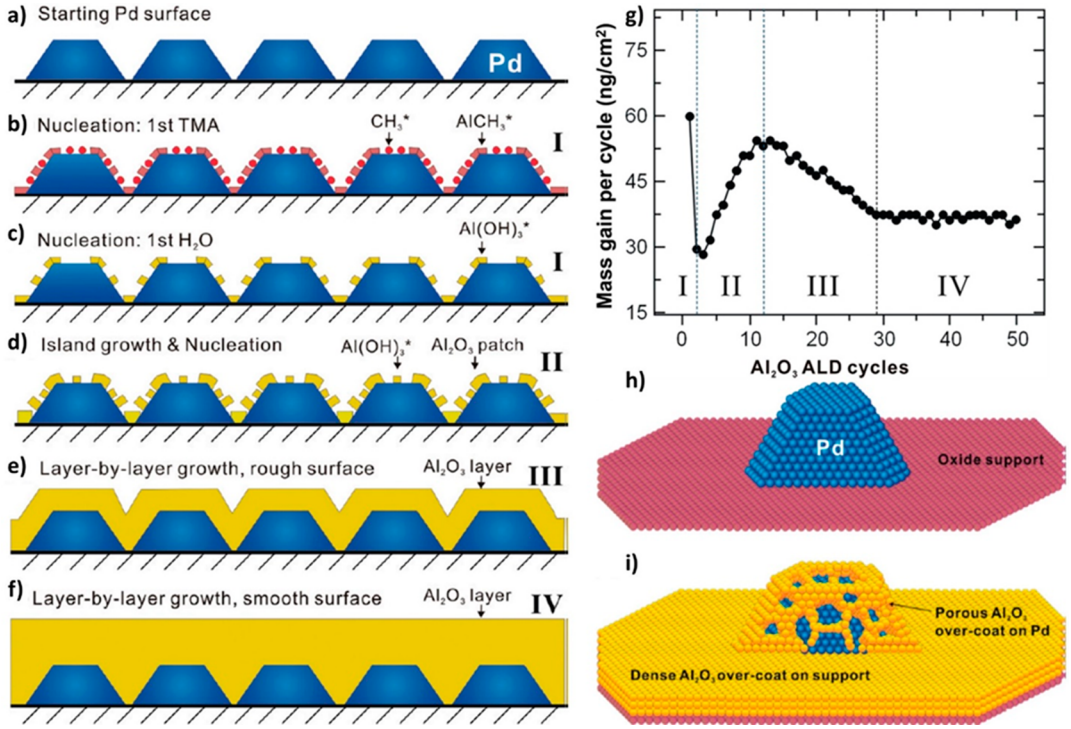

Figure 2. (a–f) Schematic illustration of the Al_2O_3 ALD growth process starting with (a) high density Pd nanoparticles on the support surface; (b) nucleation via TMA begins selectively at corner and edge sites; (c) first H_2O exposure; (d) three-dimensional growth of the initial nucleation sites; (e) growth continues and islands merge to form a continuous layer; (f) growth continues and surface roughness from the Pd nanoparticles has dissipated. (g) Al_2O_3 mass gain per ALD cycle divided into four growth regimes picture in panels b–f. (h) Illustration of Pd nanoparticles on oxide support and (i) the same materials with an Al_2O_3 overcoating with dense layers on the support and porous overcoating on the Pd nanoparticles. Reprinted with permission from ref 18. Copyright 2012 American Chemical Society.

materials, the application, and the working temperature of the catalyst.[51,52]

2.1. ALD Overcoating Mechanism and Examples. Recently, researchers have begun to utilize ALD coatings on a variety of different SMN catalysts. ALD overcoated catalysts have shown more excellent stability by suppressing sintering and coke formation, which increase the lifetime of the catalyst and improve catalytic activity.[1,9,40−43,45,53,54] Along with improving stability through the suppression of sintering and coke formation, an overcoating can also tune catalyst selectivity and introduce new active sites through unique surface chemistry interactions. The self-limiting nature of the ALD process also allows for high precision during the deposition of the coating. This makes the application of an overcoating layer via ALD equally viable on flat substrates versus porous solids with a high surface area. The ALD process is also quite versatile as the deposition of many different oxides (e.g., Al_2O_3, TiO_2, SiO_2, MgO, MnO, ZnO, ZrO_2, Fe_2O_3, CeO_2, La_2O_3, Nb_2O_5) and metal phases (e.g., Co, Ni, Pt, Pd, Ru, Rh) have been successfully demonstrated.[55−58]

Although ALD is commonly thought of as a thin-film deposition technique, various growth regimes exist based on the specific ALD chemistry, such as nanoparticle formation and discontinuous "islands". As mentioned earlier, the nature of the ALD process allows for total conformal deposition on a substrate. However, research has shown that specific substrates can result in selective, noncontinuous growth of the ALD overcoating. For example, Lu et al. monitored the growth of an Al_2O_3 overcoating on Pd nanoparticles supported on an oxide substrate.[18] In the initial ALD cycles that nucleation occurring via trimethylaluminum (TMA) dissociative adsorption was favored at Pd edge and corner sites. A schematic illustration of the growth process can be seen in Figure 2a–f. In situ quartz crystal microbalance (QCM) measurements were also used to study the mass gain per ALD cycle (Figure 2g). The QCM results were consistent with substrate-inhibited ALD growth, a process in which growth begins islands forming at discrete sites before eventually forming a continuous film. An illustration of bare and overcoated Pd nanoparticles can be seen in Figure 2h,i, respectively.[59,60] The research showed that the Al_2O_3 overcoating layer does not grow in a continuous layer, as is expected with ALD, but instead favors growth on the Pd nanoparticles' specific sites. Experimentally, work by Elam et al. also showed, using diffuse reflectance infrared Fourier transform spectroscopy (DRIFTS), that an Al_2O_3 overcoating preferentially nucleates at corners, edges, and steps of Pd nanoparticles.[54] DRIFTS was applied to study the carbon monoxide (CO) chemisorption on the Pd nanoparticles. Characteristic CO peaks at specific Pd sites were compared for samples with and without an Al_2O_3 overcoating. As the number of ALD cycles increased, the CO−DRIFTS data showed that the TMA precursor reacts with surface hydroxyl groups (as intended) and at the most active Pd nanoparticles (e.g., corner and edge sites). During the methanol decomposition process, dehydrogenation rapidly occurs at Pd (111) sites. In contrast, edge, step, and corner sites catalyze the C−O breakage, resulting in adsorbed carbon species (i.e., coke).[61,62] This process provides insight into how the ALD overcoating increases catalytic selectivity by blocking the energetic Pd sites, which prevents coke formation and still leaves the catalytically active Pd (111) sites accessible. The application of an oxide overcoating on metal nanoparticles results in 2D interfaces

https://dx.doi.org/10.1021/acscatal.0c05099
ACS Catal. 2021, 11, 2605−2619

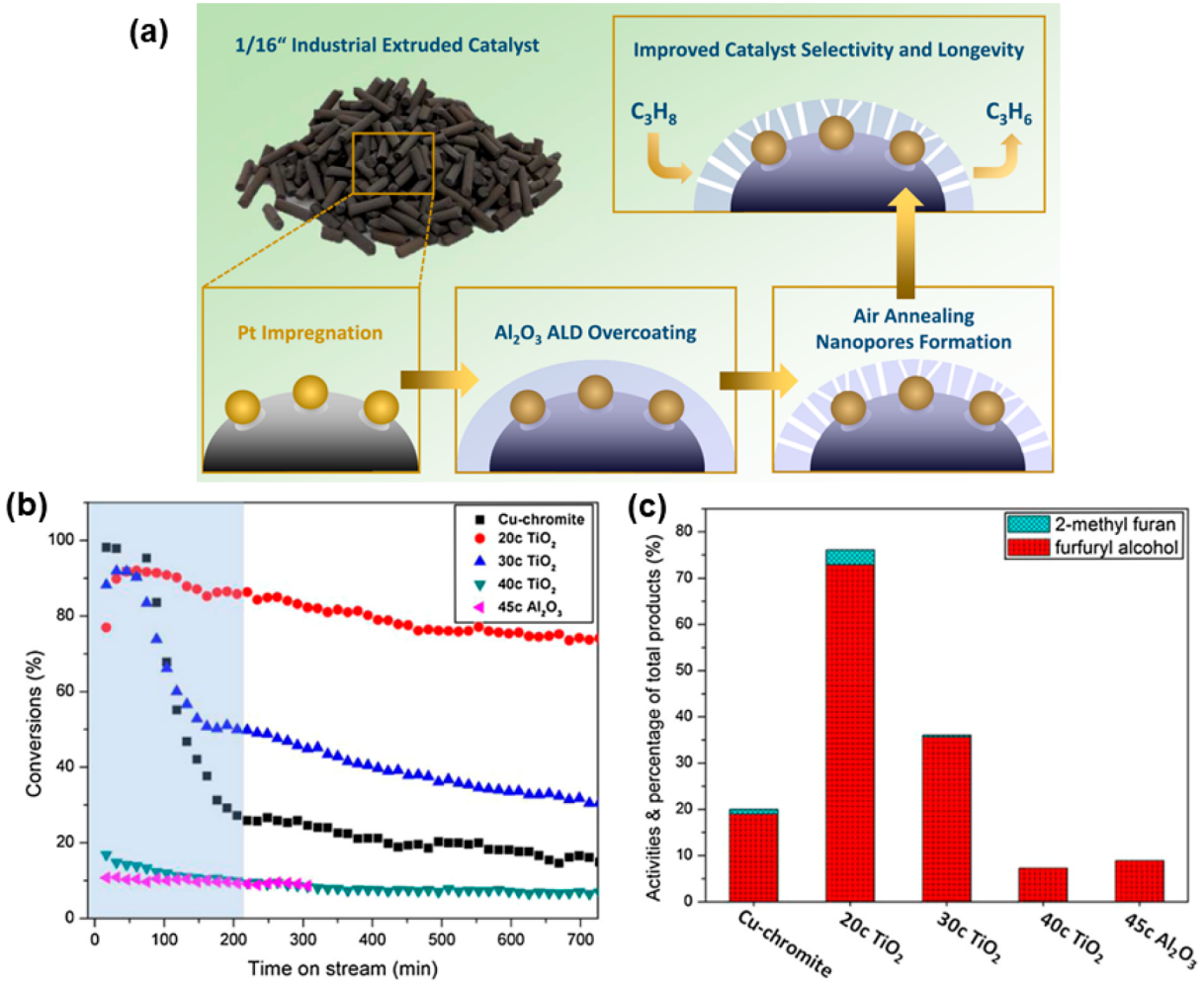

Figure 3. (a) Schematic of Al_2O_3 ALD overcoating on 1/16 in. industrial extruded Pt catalyst. Reprinted with permission from ref 69. Copyright 2020 American Chemical Society. (b) Conversion percentage as a function of time. (c) Activity and product percentages comparing different coating thicknesses on Cu-chromite catalysts. Reproduced with permission from ref 41. Copyright 2015 Elsevier.

becoming 3D interfaces which has been shown to improve metal stability.[63,64] Oxide overlayers can be preferentially deposited so that active metal sites exist at the metal-oxide interface. This has shown to greatly increase catalytic activity.[65,66] Cao et al. utilized the atomic level precision of ALD to deposit atomically dispersed $Fe_1(OH)_x$ species on Pt nanoparticles on a SiO_2 support.[67] The overcoated catalyst was then compared to traditional catalysts by measuring their performance in preferential oxidation of CO in H_2 (PROX) reactions. The catalyst with 1 cycle of the FeO_x overcoating demonstrated a CO selectivity rate of 100% with complete CO removal. The overcoated catalyst was also able to operate at this efficiency within an unprecedented temperature range of −75 to 107 °C, while the uncoated catalyst only reaches a peak efficiency of ∼80% above 400 °C. Computational studies have also confirmed that an overcoating deposition via ALD preferentially decorates the low-coordination, high energy sites of metal nanoparticles. DFT calculations were combined with experimental microkinetic analysis to study the ALD of metal oxides using metal cyclopentadienyl precursors (MCp_2, M = Fe, Co, and Ni). It was shown that the preferential decoration on step edges of Pd and Pt nanoparticles is related to the differences in the free energy change on the (111) and (211) surfaces and the deposition and that the MCp_2 followed the order of edge > (100) > (111), in which edges were covered first.[68] Lu et al. also confirmed the preferential deposition on Au nanoparticles during the ALD of a TiO_2 overcoat.[47] Qin et al. demonstrated that the ALD of FeO_x using ferrocene and O_3 as precursors preferentially decorated Pt nanoparticle's low coordination sites. The FeO_x overcoating also improved the selectivity (45% to 84%) of cinnamyl alcohol for the hydrogenation of cinnamaldehyde.[48]

Lu et al. applied a 45 ALD cycle (45c) alumina overcoating to supported Pd nanoparticles and found that the overcoating significantly reduced catalyst deactivation by sintering and coking for the oxidative dehydrogenation of ethane at 675 °C.[18,26] High-resolution transmission electron microscopy (HR-TEM) images showed that the Al_2O_3 overcoat thickness was 7.7 nm. Because of the high thickness of the overcoating, all Pd nanoparticles were covered entirely, as confirmed by CO chemisorption data. After calcination at 500 °C in O_2, CO chemisorption peaks returned but became more pronounced after increasing the calcination temperature to 700 °C, which is crucial for exposing the Pd active sites and restoring the catalytic activity. Scanning transmission electron microscopy was then used to determine the effect of the overcoating on the thermal stability of the Pd nanoparticles. The uncoated Pd/Al_2O_3 sample had an initial average particle size of 2.8 nm,

https://dx.doi.org/10.1021/acscatal.0c05099
ACS Catal. 2021, 11, 2605−2619

which increased to 4.6 nm after undergoing reactions for only 30 min. The change to a broader, larger particle distribution was attributed to sintering. However, the 45c overcoated Pd/Al_2O_3 showed an initial average particle size of 2.8 nm, which was unchanged after 1700 min of catalysis. For the uncoated catalyst, coke formation cause yields to drop to zero within 30 min of the reaction. In contrast, the overcoated catalyst showed improvements in ethylene yield and was catalytically stable for ~1700 min. Infrared spectra of CO chemisorption confirmed that the ALD Al_2O_3 overcoating preferentially blocked the low-coordinated Pd catalyst sites. Such sites typically favor the C−C bond scission and hydrogen stripping, which produces the C fragments that lead to coke, CO, CH_4, and CO_2. The preferential blocking of low-coordinated sites also explains the catalyst stability improvement since Ostwald ripening occurs as low-coordinated surface metal atoms are released to form larger particles. The stabilization of SMN using alumina overcoating by ALD has also been proved to be successful on industrial catalysts by Lu et al., as shown in Figure 3a.[69] The catalysts are Pt nanoparticles dispersed on 1/16 in. Al_2O_3 extrudates with different surface area. They investigated the interplay of Pt loading, ALD overcoat thickness, and Al_2O_3 support surface area on propane dehydrogenation selectivity and catalyst stability. With the increase of the ALD Al_2O_3 cycles, both catalyst stability and propylene selectivity were improved. This study demonstrated that the Al_2O_3 ALD overcoats were used to selectively block the inactive metal sites and stabilize the Pt nanoparticles from sintering by forming an Al_2O_3 physical barrier.

Considering the high price of noble metals, it will be cost-effective to utilize nonprecious metals such as Cu, Co, and so on. For example, copper chromite as a catalyst has been shown to be effective for the selective hydrogenation of 2-furfuraldehyde.[41,70] This catalyst suffers from deactivation due to chromium migration over copper atoms and coke formation. Zhang et al. demonstrated that applying a thin film of Al_2O_3 via ALD could increase catalyst stability for the gas-phase hydrogenation of 2-furfuraldehyde. With 10 cycles of the Al_2O_3 overcoating, the catalyst showed improved stability with little to no deactivation after 5 h under reaction conditions. Another catalyst was also prepared using a TiO_2 ALD overcoating, which showed a substantial improvement compared with the Al_2O_3 overcoated catalyst. The catalyst with 20 cycles of TiO_2 ALD preserved roughly 75% activity after 700 min on stream, as seen in Figure 3b. The stability of the catalyst based on ALD cycles can be seen in Figure 3c, which shows the activity and product composition after 500 min on stream. The drastic increase in activity was attributed to the weaker interaction between copper chromite and the TiO_2 compared to the Al_2O_3 overcoat. Alba-Rubio et al. found that the acidic Al_2O_3 ALD resulted in forming a bifunctional metal-acid catalyst.[25] Furfuryl butyl ether was formed due to the overcoat's acidity layer, which catalyzed furfuryl alcohol's etherification with 1-butanol. In a proof-of-concept experiment, the more acidic NbO_x was deposited via ALD, which led to the further formation of new acid sites and increased the etherification rate by order of one magnitude. Recent work has also shown the benefit of an ALD overcoating when applied to the cathode in a solid oxide fuel cell. A ZrO_2 overcoating was applied to the $La_{0.6}Sr_{0.4}CoO_{3-\delta}$ (on a $La_{0\ 0.8}Sr_{0\ 0.2}Ga_{0\ 0.83}Mg_{0\ 0.17}O_{3-\delta}$ support) cathode and was shown to stabilize the $La_{0.6}Sr_{0.4}CoO_{3-\delta}$ particles by suppressing Sr segregation at the surface of the cathode. The stability effect was demonstrated by retaining the activity of the oxygen reduction reaction (ORR) for over 4000 h at 700 °C, which is an improvement in the performance of the new materials by a factor of 19.[71]

Many studies have shown that the ALD overcoating can also improve the catalyst stability in aqueous-phase reactions. When trying to stabilize cobalt catalysts for the aqueous-phase hydrogenation (APH) reaction, Lee et al. demonstrated the importance of selecting a coating material.[9] The Co catalyst was testing with Al_2O_3 and TiO_2 ALD coatings. The Al_2O_3 overcoated catalyst showed no catalytic activity because of an irreducible cobalt aluminate phase forming. However, the TiO_2 coated catalyst was able to stabilize the Co catalyst by preventing sintering and leaching.[9] Because of stability issues, precious metals such as Pt and Ru are typically used for these reactions. This research opened the door for new, low-cost catalysts such as Co coupled with an ALD overcoating. The application of an Al_2O_3 overcoating has also been shown to be successful for stabilizing supported copper catalysts for the hydrogenation of 2-furfuraldehyde in liquid-phase reactions.[7,25,45] Lei et al. applied ZnO ALD overcoating to promote Pt catalysts for aqueous-phase reforming of 1-propanol.[72] The enhanced activity and selectivity after ZnO overcoating derived not only from the protecting morphological structure but also from the Zn → Pt charge transfer. This study demonstrated the overcoat material could function as a promoter as well.

Similar to ALD, molecular layer deposition (MLD) is also based on self-limiting and sequential surface reactions in the gas phase. It is also a useful technique for generating thin film but differs in that organic precursors are used to create polymers or organic−inorganic hybrid films. For example, the MLD of alucone, an aluminum-based hybrid organic−inorganic film, used TMA and ethylene glycol (EG, HO-$(CH_2)_2$−OH).[34,35,44] The general procedure is the same as Al_2O_3 ALD with the only difference being that EG is used in place of H_2O. Because of MLD's ability to deposit hybrid materials and polymers with precise layer-by-layer control, various metalcones have been developed for various applications.[73−77] Also, with MLD, it is crucial to generate pores within the overcoating to allow access to active sites. One technique for pore generation involves removing the organic components with the MLD layers by water etching or thermal treatment.[78] The residual structure results in porous layers which allow access to metal sites while preventing metal sintering. Gould et al. used MLD to prepare a porous alucone layer to prevent Ni nanoparticles' sintering used for the dry reforming of methane (DRM).[44] Under the harsh DRM conditions, Ni nanoparticles without the MLD overcoating increased in size from the initial 5.3 to 9.7 nm after 82 h. In contrast, the Ni particles with 10-cycle MLD (~2.4 nm thick) increased to an average of only 7.8 nm after 108 h and two additional reduction/calcination cycles. It was also noted that the addition of the overcoating cut the amount of coke formation in half. Ingale et al. compared the difference in overcoating effects between Al_2O_3 via ALD and alucone via MLD on Ni catalysts for the DRM.[79] They noted that the Al_2O_3 ALD Ni catalysts showed little to no increase in stability or activity, likely due to inactive $NiAl_2O_4$ species' formation blocking the DRM active Ni^0 sites. In contrast, the alucone MLD overcoating showed high activity and increased stability under DRM conditions. It was shown that the MLD overcoating after only three cycles had a significant effect on

https://dx.doi.org/10.1021/acscatal.0c05099
ACS Catal. 2021, 11, 2605−2619

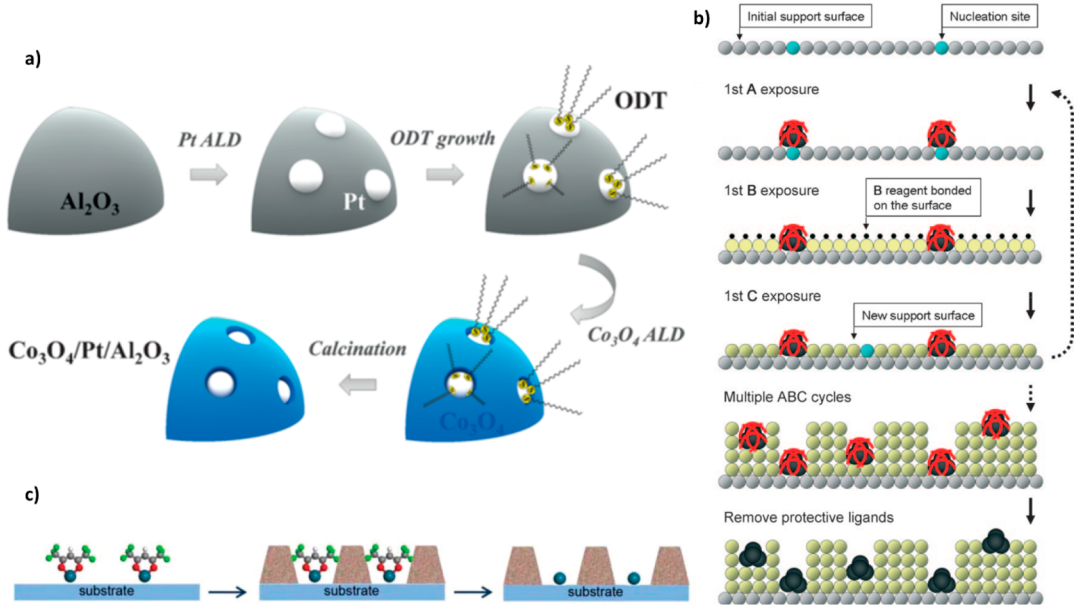

Figure 4. (a) Illustration of the preparation of ALD Co_3O_4 nanotraps for stabilizing supported Pt catalyst. Reproduced with permission from ref 84. Copyright 2017 Wiley-VCH Verlag GmbH & Co. KGaA, Weinheim. (b) Schematic illustration of the ABC-type ALD process. Reproduced with permission from ref 85. Copyright 2010 Wiley-VCH Verlag GmbH & Co. KGaA, Weinheim. (c) Representation of the ALD Al_2O_3 nanobowl formation for stabilizing Pd single-atom catalysts. Reproduced with permission from ref 86. Copyright 2016 Royal Society of Chemistry.

Ni stability and allowed the catalyst to operate at higher temperatures without sintering. Piper et al. utilized alucone thin film on Si nanoparticles as part of the anode in a lithium-ion battery (LIB). The MLD coated anode outperformed the uncoated cathode by boasting a specific capacity of 900 mAh g^{-1} after 150 cycles, while the anode without the coating layer rapidly degraded and failed after 30 cycles.[80]

2.2. Stabilization of Metal Nanoparticles by Area-Selective ALD. For SMN catalysts, the metal particles' size plays a large role in determining catalytic selectivity and activity. Various techniques have been employed for nanoparticle synthesis, including ALD, precipitation, laser-assisted desorption, impregnation, and colloidal synthesis, each of which has its advantages and disadvantages. Research has shown that the ideal nanoparticle size varies for each application, and each system has unique interactions between the metal, support, and overcoating layer of SMN catalysts. The general idea for preparing supported metal nanoparticles is that small particles offer a higher number of surface-active atoms per weight percentage but lower thermal stability as particle size decreases. One of the key challenges is controlling and minimizing metal nanoparticles' size when it comes to the synthesis and stabilization of new SMN catalyst systems. Bo et al. utilized surface-modified TiO_2 support particles that were partially masked with a thin SiO_2 overcoating for an Ag-based SMN catalyst.[22] The modified TiO_2 surface and the SiO_2 coating created a template in which Ag nanoparticles were deposited via photodeposition. The overcoating based template resulted in the deposition of uniform Ag nanoparticles with diameters $\leq$3.5 nm. In contrast, Ag particles deposited on the unmodified TiO_2 support were larger (4.7 $\pm$ 2.7 nm) and more polydisperse. Additionally, the samples containing the SiO_2 coating showed no signs of sintering after being heated to 450 °C for 3 h, while large Ag aggregates (>10 nm) were observed in the uncoated sample. The lack of sintering in the coated sample was partially attributed to the strong binding interaction between the TiO_2 and Ag nanoparticles, and the fact that the nanoparticles weakly interact with the SiO_2 domains creates an energetic barrier preventing nanoparticle aggregation.[81,82] In this case, the additional overcoating layer facilitates the deposition of the smaller, more uniform nanoparticles while also providing increased particle stability at high temperatures.

Ray et al. demonstrated four useful blocking agents (nitriles, amines, thiols, and the ligand hexafluoroacetylacetonate) as a protective layer on Pd nanoparticles during the ALD of Al_2O_3 an overcoating.[83] It was shown that the thiols and amines have the highest binding affinity and protection for the Pd nanoparticles. Liu et al. utilized selective-area ALD to generate oxide nanotraps to secure platinum nanoparticles on Al_2O_3 support.[84] In this work, 1-octadecanethiol (ODT) was used as a protecting agent on the Pt nanoparticles because of the strong binding strength between the thiol group and Pt. A Co_3O_4 overcoating was then applied via ALD to the surface of the Al_2O_3 support. The materials were then calcined in air to remove the ODT protecting group resulting in the formation of Co_3O_4 nanotraps that contained the Pt nanoparticles, as seen in Figure 4a. The Pt−Co_3O_4 interface interactions resulted in a decrease in the CO oxidation temperature and activation energy required. It was also noted that the thermal stability of the Pt nanoparticle increased. After undergoing calcination at 600 °C in air, an average Pt particle size was determined to be 2.91 nm for the sample containing the Co_3O_4 nanotraps, while the sample without the nanotraps had an average particle size of 9.74 nm.

Techniques have also been developed to simultaneously synthesize highly dispersed nanoparticles protected by a metal oxide overcoating. Lu et al. utilized an ABC-type method (Figure 4b) in which the protecting group ligands were from the ALD precursors.[85] Initially, the precursor palladium hexafluoroacetylacetonate ($Pd(hfac)_2$) was deposited on the support material, while the hfac ligands remained on the Pd. The next precursor, TMA, was then introduced to react with surface hydroxyl groups followed by H_2O to form an Al_2O_3

https://dx.doi.org/10.1021/acscatal.0c05099
ACS Catal. 2021, 11, 2605−2619

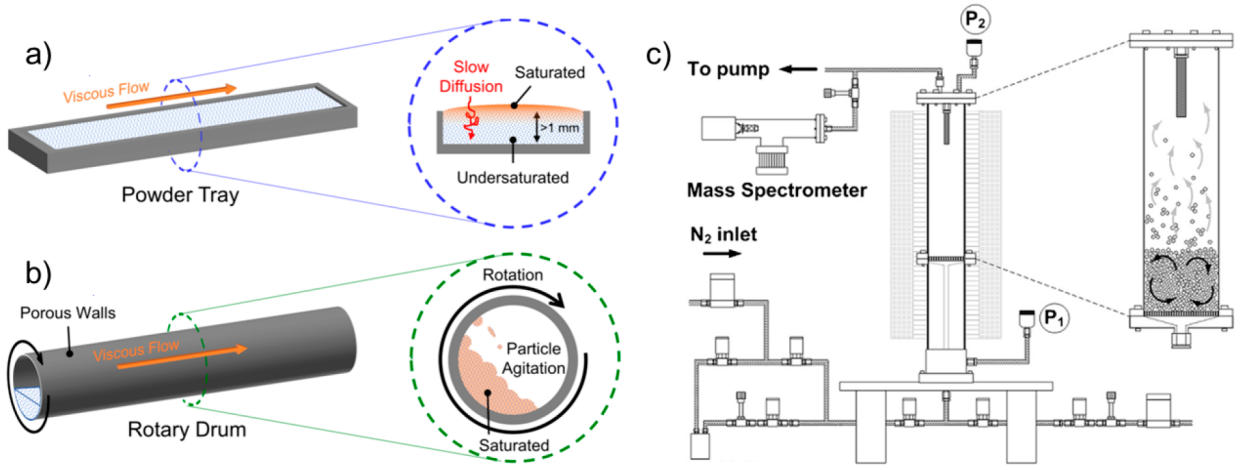

Figure 5. Schematic depiction of (a) stainless-steel tray containing powder catalyst and (b) rotary drum ALD reactor. Reprinted with permission from ref 95. Copyright 2020 American Vacuum Society. (c) Fluidized bed ALD reactor. Reprinted with permission from ref 96. Copyright 2008 Elsevier B.V.

overcoat on the support. The hfac ligands protect the Pd from reacting with the Al_2O_3 precursors so that the Al_2O_3 is only deposited on the support material and not the Pd. After the desired density of protecting Pd nanoparticles and Al_2O_3 overcoating is achieved, the hfac ligands are removed by calcination leaving the Pd nanoparticles exposed. This direct synthesis route offers a unique approach for synthesizing highly uniform SMNs with high catalytic stability. Lei et al. utilized $Pd(hfac)_2$ as a precursor to synthesize protect single-atom Pd catalysts.[86] First, $Pd(hfac)_2$ is chemisorbed onto the substrate surface. A thin film of TiO_2 was then applied via ALD, which only deposits on the substrate surface and not the $Pd(hfac)_2$ due to the hfac ligands' presence. The bulky nature of the ligands results in the formation of nanobowls around the protected Pd sites. Lastly, the hfac ligands are removed via formalin (HCHO). A schematic illustration of the synthesis process can be seen in Figure 4c. Overall, the TiO_2 overcoating greatly increased the single-atom Pd's stability during both reduction and oxidation conditions and was shown to be a promising catalyst for methanol decomposition reactions.

The research mentioned above briefly demonstrates the versatility of ALD-based overcoating and how they can be applied to stabilize a variety of different catalysts. For the overcoating that is at least one atomic layer, the formation of the nanopores allows access to the catalytic sites so that the catalyst materials can retain their activity. Although the process is not fully understood, there has been progress in the past few years related to understanding the mechanism of pore formation. During the calcination process, research has shown that pore formation can be affected by the type of overcoat and support material, catalyst size, overcoating thickness, catalyst composition, heating environment, and heating rate.[24,87]

The thickness of the overcoating layer typically describes by the number of ALD cycles, has also been shown to play a significant role in affecting catalyst stability and activity. As mentioned above, the ideal overcoating thickness is highly dependent on the specific application. A typical range for the deposition of an overcoating layer is between 5 and 45 ALD cycles. The actual thickness of the overcoating will vary depending on the ALD material. In general, catalyst stability will increase as the number of ALD cycles increases, but an overly thick coating can result in catalytic activity loss. O'Neill et al. prepared Cu catalysts supported on a γ-Al_2O_3 support with 5, 15, and 45 cycles ALD AlO_x overcoating.[53] The materials then underwent calcination at two different temperatures before their catalytic rates for furfuryl and furfural alcohol production were measured. In this work, the thinnest coating at 5 ALD cycles offers the highest catalytic activity while having the same degradation rate as the catalysts with overcoating of 15 and 45 ALD cycles. It was shown that fully regenerable Cu catalysts for liquid-phase hydrogenation reactions could be attained with only 5 cycles of AlO_x overcoating. However, for higher calcination temperatures, the 45-cycle overcoating has a much lower loss in activity compared with the 5-cycle overcoating.

The support material used for SMN catalysts can also have a large effect on short and long-term catalytic activity. The support materials serve not only as a scaffold for the metal catalyst but can also affect catalyst selectivity and activity in a variety of ways, including changing surface acidity/basicity, creating new active sites, altering the electronic structure of the active sites, changing morphology and size of the metal nanoparticles, and encapsulating the metal nanoparticles via metal−support interactions.[88−91] Breaking down different support materials into two major categories, we can describe them as either porous or nonporous. It is essential to note the pore formation in the ALD overcoating during calcination is not dependent on the type of support material, though it can affect the number and physical properties of overcoating pores. Recent work by George et al. prepared 1 nm Pd nanoparticles on two different support materials to investigate different effects of an ALD overcoating.[24] The catalyst nanoparticles were featured on both spherical, 60 nm Al_2O_3 particles and Al_2O_3 porous particles with broad distribution aggregate particles and pore sizes. Each material then underwent AlO_x ALD for 20, 30, or 40 cycles at temperatures of 100, 200, or 300 °C, respectively. A set of overcoated samples was also prepared for each support material without adding the Pd nanoparticles. After samples were calcined to 800 °C, the pore size, volume, and distribution were analyzed via N_2 physisorption. Most notably, a tunable relationship was identified between the pore volume and the ALD temperature. For samples without Pd nanoparticles, the nonporous support

https://dx.doi.org/10.1021/acscatal.0c05099
ACS Catal. 2021, 11, 2605−2619

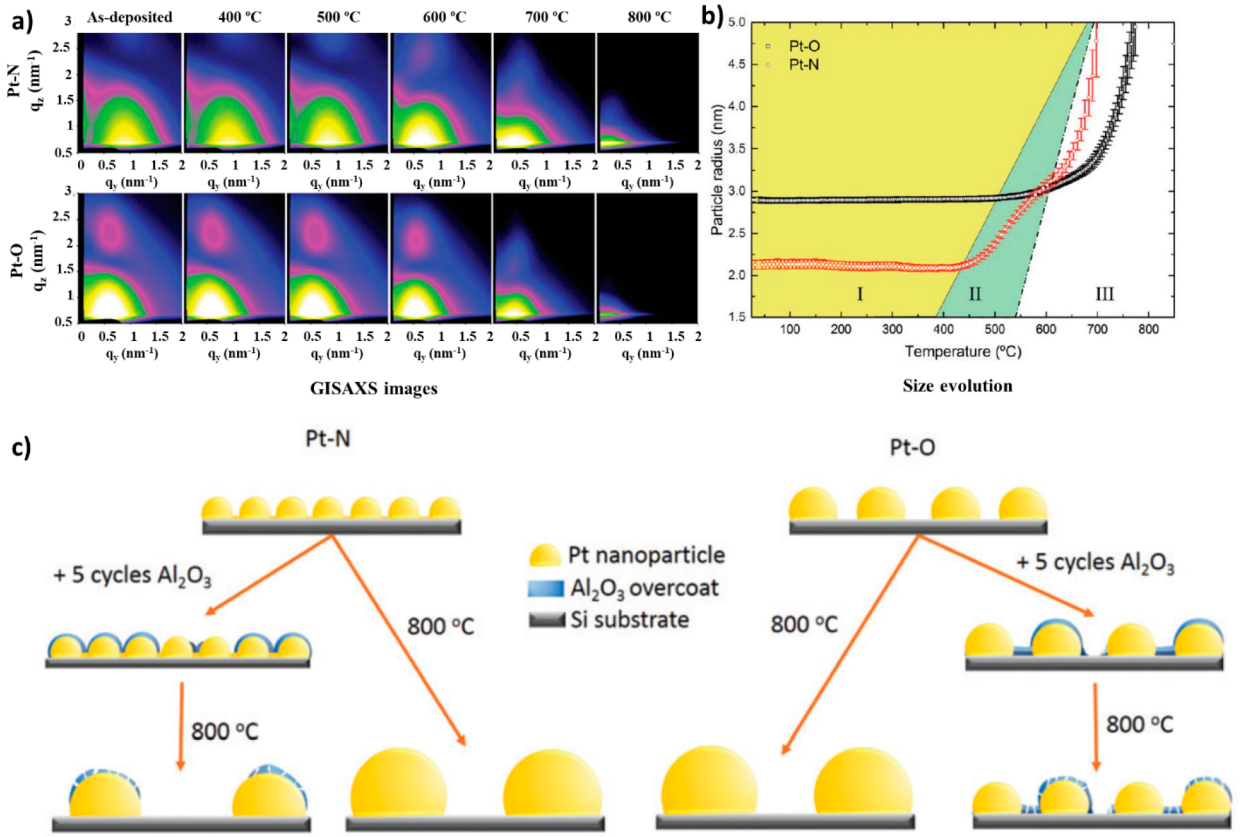

Figure 6. (a) GISAXS images and (b) the calculated Pt particle size via GISAXS images as a function of temperature for (a) Pt−N samples and (b) Pt−O samples. (b) Representation of particle evolution for Pt−N and Pt−O samples with and without an Al_2O_3 overcoating. Reproduced with permission from ref 97. Copyright 2020 Royal Society of Chemistry.

showed a lower volume of small pores around 2 nm were present in the ALD films deposited at higher temperatures. In contrast, porous supports contained a high volume of small pores and greater surface area. It was noted that this feature was due to less residual H_2O remaining in the porous support material during ALD at higher temperatures, which results in pores not being filled in the support material.[92,93] For the samples containing Pd nanoparticles, the same trend was observed with an increased number of small pores.

2.3. ALD Tools and Methods to Coat Catalyst. It has already been proved that ALD is capable of depositing material with high precision; however, when coating the catalyst with high surface area, the ALD equipment and process are different compared with those used for planar coating substrates. Since the precursors and products' diffusion rate into and away from reaction sites within the porous structure is relatively slow, it is essential to redesign the ALD process and reactor for effective powder coating.

When the powder quantity is small (e.g., 1−10 g), the conventional ALD system can still be used by spreading the powder uniformly inside a stainless-steel tray with a mesh on top. The mesh's pore size is smaller than the powder particle size to prevent powder spilling but still allows efficient diffusion of the ALD precursors and byproducts in and out of the tray.[57,94] To fulfill the precursor's adequate penetration deep inside the powder bed vertically, a long precursor dose and purge time are required. However, it is often observed that the powder at the bottom of the tray is unsaturated, resulting in nonuniform ALD coating, as shown in Figure 5a. Thus, specialized ALD systems, such as fluidized bed, rotary drum, or spatial ALD reactor, are developed.

Figure 5b shows the schematic of a rotary drum incorporated in a hot-walled, viscous flow ALD reactor. The rotary drum is connected to a motor, which allows the particles to be agitated while performing the ALD coating.[95] Instead of using an external force to agitate the powder, Figure 5c shows the fluidized bed reactor's schematic. The powder is contained inside a vertical tube, and the carrier gas is injected from the bottom. When the upward drag force exerted by the carrier gas is equal to or larger than the gravity of the powder, those powder particles will be fluidized.[96] Rotary drum and fluidized bed ALD reactors can facilitate the heat and mass exchange and overcome diffusion limitations when coating a larger quantity of powder.

3. CHARACTERIZATION

Understanding the process of pore formation in the overcoating will allow for better control of pore formation and the structural changes associated with pore formation during the calcination process. A better understanding of the catalyst overcoating layer will significantly benefit the synergistic effects between the overcoating and catalyst itself. This will eventually lead to a better catalyst design for highly efficient and stable materials. The ability to fully characterize overcoated catalysts is another aspect of this topic that cannot be understated. Overcoated SMN catalysts contain a support material, metal nanoparticles, and the overcoating layer. All of which can have unique interfacial interactions and surface chemistries based on the type of materials. Because of their complicated nature and

https://dx.doi.org/10.1021/acscatal.0c05099
ACS Catal. 2021, 11, 2605−2619

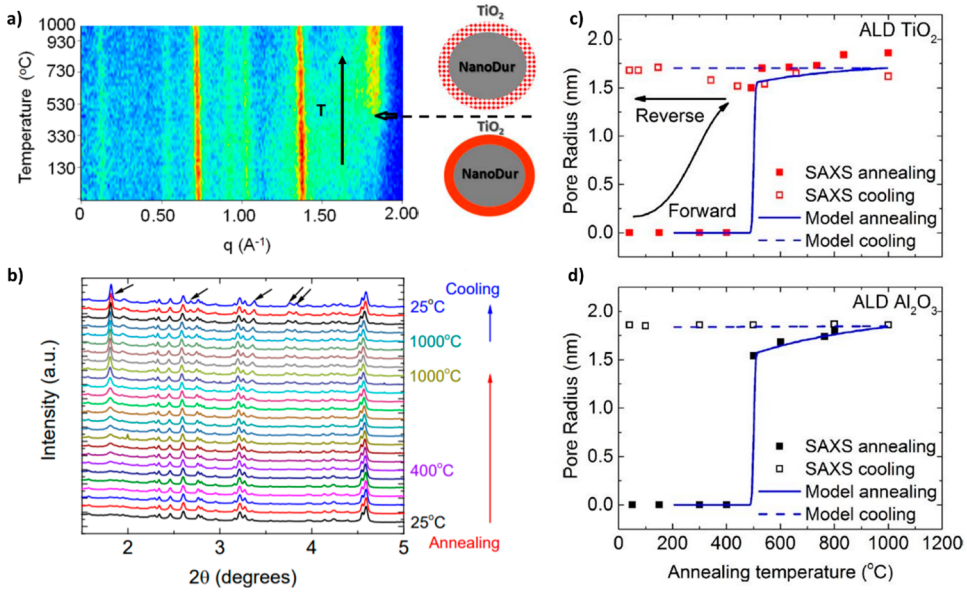

Figure 7. (a) Contour plot of the combined in situ SAXS/WAXS data. The dotted line shows the phase transition as a function of temperature resulting in pore formation in the TiO_2 overcoating. Reproduced with permission from ref 100. Copyright 2016 American Chemical Society. (b) In situ XRD data for the TiO_2 overcoated sample as a function of temperature. In situ SAXS data and mathematical model describing ALD film pore size as a function of temperature for the ALD (c) TiO_2 and (d) Al_2O_3 overcoating. Reproduced with permission from ref 87. Copyright 2018 American Vacuum Society.

the fundamental properties of a catalyst, in operando/in situ characterization of SMN catalysts are vital.

Recent work done by Solano et al. utilized ALD to fabricate Pt nanoparticle on a Si substrate to investigate nanoparticle thermal stability as a particle size function.[97] Two different samples were prepared by depositing Pt via ALD using a nucleation regime of either O_2 or N_2 (N_2*) plasma. Each of the two samples contained an equal amount of Pt but varied in particle coverage and size. For clarity, the samples generated using the O_2 plasma and N_2 plasma will be referred to as Pt−O and Pt−N, respectively. This method resulted in a distinct difference in Pt particle size where the radius of the Pt−O particle was 3.2 nm, while the Pt−N particles were smaller with a radius of 2.1 nm. Samples were then prepared with various ALD cycles of an Al_2O_3 overcoating before being heated to 850 °C (0.2 °C s^{-1}). Pt particle size was monitored as a function of temperature, as seen in Figure 6a,b, via in situ grazing-incidence small-angle X-ray scattering (GISAXS). GISAXS has shown to be a powerful tool for determining the size/shape of nanosized materials in thin films, at surface interfaces, and at the surface of materials.[98,99] In situ low-energy ion scattering (LEIS) was also used to determine the atomic composition at the surface of the select sample. The GISAXS and LEIS data show that as few as one ALD cycle of Al_2O_3 has a large effect in protecting the Pt particles against sintering. The data also showed that the more isolated Pt−O nanoparticles were less susceptible to coarsening than the Pt−N nanoparticles. This was due to the Pt−N nanoparticles' high surface density, which prevented the physical particle isolation by the Al_2O_3 overcoating (Figure 6c).

Many industrial SMN catalysts operate in specific atmospheres, temperatures, and pressures. To fully understand a catalytic reaction, in operando characterization methods are vital as they can monitor structural, chemical, and electronic changes to materials during catalysis. For fresh, unused overcoated SMN catalysts, structural changes typically occur at elevated temperatures during the calcination process.[7,25,100] Specifically, it is essential to monitor the metal nanoparticle for any changes resulting in sintering along with changes in the overcoating layer resulting in the formation of nanopores. For many catalysts, the calcination temperature is often required to be at or above 500 °C. Monitoring structural changes at such elevated temperatures often require specialized equipment and are outside the capabilities of many lab instruments. Typical methods for characterizing porous materials such as Barret−Joyner−Halenda (BJH) and Brunauer−Emmett−Teller (BET) theory lack the ability for time-resolved data acquisition for in-operando conditions. Recent research by our group analyzed the structural changes that occurred in TiO_2 and Al_2O_3 overcoating on nonporous support.[100] This work was able to monitor overcoating pore formation using specialized sample cells combined with synchrotron-based X-ray techniques. Pore formation and evolution were monitored using small-angle (SAXS) and wide-angle (WAXS) X-ray scattering. First, the Al_2O_3 ALD overcoated support was calcined to different temperatures with a maximum of 800 °C while measuring the sample with SAXS. At lower temperatures (300 °C), no changes were observed; however, the maximum temperature changes in the SAXS spectra were visible. After data treatment and fitting, the SAXS data showed pores' formation with a size range of around 10 nm. The SAXS data for the TiO_2 coated sample showed that pore formation occurred around 500 °C, resulting in 2.5 nm pores. Based on the assumption that pore formation is based on the overcoating layer's densification, high-resolution X-ray diffraction (HRXRD) was then used to identify structural changes during heating. The HRXRD data was consistent with the SAXS data in that changes were only observed at the same elevated temperatures for each overcoating material. Analysis of the XRD pattern showed the formation of sharp diffraction peaks at the same temperatures that changes in the SAXS spectra were observed, indicating the overcoating change from amorphous to

https://dx.doi.org/10.1021/acscatal.0c05099
ACS Catal. 2021, 11, 2605−2619

crystalline. To confirm these results and provide insight into the pore opening process, a TiO_2 overcoated sample was measured via in situ SAXS/WAXS. The sample was heated from 30 to 1000 °C at a rate of 20 °C/min with SAXS and WAXS images taken every 60 s. Figure 7a shows a contour plot of the combined SAXS and WAXS data. The figure shows a sharp intensity increase at q value 1.83 $Å^{-1}$ representing a peak formation due to the transition to the anatase phase of TiO_2. By looking at the peak area as a function of temperature, the sharp phase transition can be clearly seen around 470 °C, denoted by the black dashed arrow in Figure 7a. The SAXS contribution from the pores in the overcoating were then isolated by subtracting the SAXS data from the uncoated sample from the overcoating spectra. The SAXS spectrum of the ALD overcoating pores can then be fit to obtain information to pore size and size distribution. The fitted data shows that pore formation occurs during the phase transition around 470 °C. It was also determined that the average pore size at 470 °C has a diameter slightly less than 2 nm. The pore size then gradually increases as temperature increases, with a final result of 2.5 nm pores developing at 700 °C. The results from this work demonstrate powerful techniques for the in situ/in operando characterization of overcoated catalyst materials. This unique look into the pore formation in ALD overcoating will help researchers design better catalyst materials.

Other recent work compared the pore formation of both TiO_2 and Al_2O_3 ALD-based overcoatings using in situ XRD and SAXS.[87] ALD overcoatings of Al_2O_3 (∼4.9 nm thick) and TiO_2 (∼2.5 nm thick) were prepared on nonporous NanoDur substrates. Samples were then subjected to in situ XRD and SAXS experiments. As seen in Figure 7b, the XRD data monitors structural changes in the ALD TiO_2 overcoated particles. The black arrows on the x-axis denote new peaks formed at temperatures above 500 °C, corresponding to the anatase TiO_2 phase transition. Figure 7c,d show the SAXS data and models for the ALD TiO_2 and Al_2O_3 overcoated particles, respectively. The plots show pore size as a function of temperature. For both overcoating materials, it was shown that pores formed abruptly around 400−500 °C. For the TiO_2 overcoating, pore formation corresponds to the temperature at which the phase transition to anatase TiO_2 was observed in the XRD data. Pore formation in the Al_2O_3 overcoating are also consistent with the phase transition from amorphous to γ-Al_2O_3.[101] It was also observed in both overcoating materials that pore size steadily increases as the annealing temperature increases (above 500 °C), meaning that pore size can be tuned by adjusting the annealing temperature. This work utilized in situ, synchrotron-based X-ray techniques to provided new insight into the pore formation mechanism in ALD overcoating materials.

As mentioned earlier, recent work by George et al. provided an in-depth look into the pore formation process in an alumina overcoating through several in situ characterization techniques.[24] In this work, AlO_x overcoating was deposited via ALD on spherical and porous Al_2O_3 substrates. For both types of support materials, pores of ∼2 nm were formed in the overcoating after high-temperature annealing. However, samples containing Pd showed an increase in small pore volume compared to films prepared without Pd. Nitrogen adsorption isotherm data was used to provide information about the overcoating pores' porosity and morphology. BJH analysis of the N_2 isotherm data showed a sharp increase at 4 nm for the pore size distribution for the N_2 desorption data. This was attributed to be an artifact caused by tensional instability of the N_2 meniscus in ink-bottle-shaped pores.[102] The dehydration of the AlO_x overcoating was also monitored via in situ thermogravimetric analysis (TGA) and DRIFTS. In situ TGA and DRIFTS data identified the loss of internal hydroxyl groups and structural water at temperatures between 500 and 650 °C. It was also shown that the addition of Pd nanoparticles resulted in a 50% increase in water in the AlO_x overcoating. It was proposed that the increase in small pore volume in the Pd containing samples was correlated to the increased water. A tunable relationship was identified between the volume of small pores and ALD temperature. For the nonporous support, ALD films that are deposited at higher temperatures result in a lower volume of small pores. In contrast, ALD films deposited on the porous support at higher temperatures resulted in a higher number of small pore and greater surface area because of less H_2O remaining in the pores at higher temperatures resulting in the incomplete filling. In situ powder X-ray diffraction (PXRD) was conducted to corroborate the structural information obtained from the nitrogen isotherm data. The PXRD spectra showed that large structural changes occurred at temperatures over 700 °C. Since structural water loss, dehydroxylation, and pore formation occur at temperatures below 700 °C, these changes correspond to the AlO_x overcoat's crystallization as Al^{3+} migrate within the oxygen lattice resulting in crystalline transition alumina. This highlights the effect of particle morphology, Pd content, and ALD temperature on pore formation in ALD thin films.

X-ray absorption spectroscopy (XAS) is a useful technique for analyzing the materials' local geometric and electronic structures.[103−106] An XAS spectrum can provide element-specific information related to the oxidation state, coordination number, and identify neighboring atoms in a sample.[107−110] XAS can investigate the structure change of the metal nanoparticles without and with ALD overcoating. In recent work, Yang et al. used XAS to analyze CuO catalysts on SiO_2.[111] Such catalysts have shown promise for use in the catalytic ozonation for water treatment but often suffer from stability issues due to leaching. To stabilize the catalyst, an Al_2O_3 thin overcoating was applied via ALD. XAS spectra were then obtained for the uncoated and ALD overcoated catalysts, as well as CuO as a reference. By analyzing the X-ray absorption near edge structure (XANES) spectra, it could first be determined that the Cu catalyst was not reduced by the addition of overcoating because of the lack of the presence of the Cu^+ characteristic peak. When comparing the XANES spectra of the fresh and used ALD catalysts, the data also showed no change in Cu's oxidation state. The Fourier transformed X-ray absorption fine structure (EXAFS) spectra were analyzed to investigate the Cu atoms' coordination number in each sample. The uncoated CuO/SiO_2 catalyst showed a Cu−O coordination number (CN) of 3.8. This CN is slightly lower than the expected CN of 4. It has been reported that the undercoordinated Cu is likely the cause of leaching in aqueous reactions.[7] After undergoing the ozonation reaction, the CN for the uncoated catalyst was reduced even further to 3.6. In contrast, the calculated CN for the fresh Al_2O_3 coated CuO/SiO_2 catalyst was 4, and the CN showed no change after undergoing the ozonation reaction. Cao et al. utilized in situ XAS to investigate Pt SMN catalysts with an atomically dispersed $Fe_1(OH)_x$ overlayer for use in proton-exchange-membrane fuel cells.[112] The iron hydroxide overlayer

https://dx.doi.org/10.1021/acscatal.0c05099
ACS Catal. 2021, 11, 2605−2619

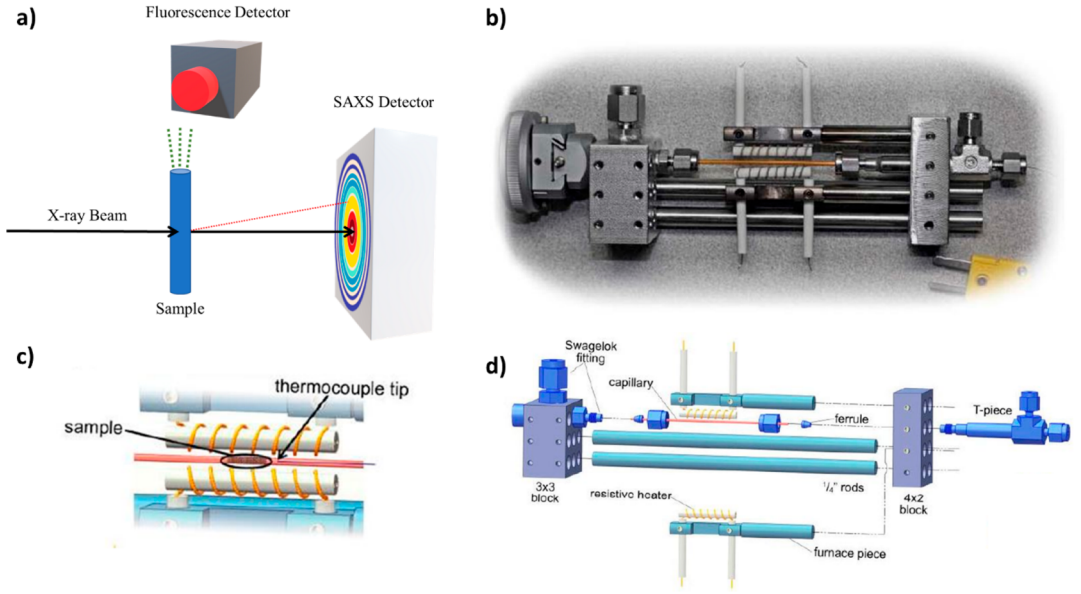

Figure 8. (a) Schematic illustration for simultaneous, in situ SAXS/XAS experiments. (b) Photo of a reaction cell designed for in situ experiments. (c) Representation of the sample holder, heating coils, and thermocouple location. (d) Expanded representational overview of the reaction cell. Reproduced with permission from ref 116. Copyright 2008 International Union of Crystallography.

had shown to dramatically increase the CO conversion rate as well as broaden the working temperature range. In situ XANES data was collected at the Fe K-edge while under 10% H_2 in helium. The XANES data showed the disappearance of a Fe^{3+} characteristic pre-edge peak while features associated with Fe^{2+} increased. The XANES data confirmed the reduction of the Fe−Pt/SiO_2 sample at room temperature, which helps explain the increased catalytic performance over the uncoated Pt catalyst. This research demonstrated the unique capabilities of an advanced characterization technique such as XAS. The XANES and EXAFS spectra were able to provide a unique insight into the fundamental role the ALD overcoating layer provided in stabilizing various SMN catalyst materials.

4. CONCLUSIONS AND OUTLOOK

In summary, we have discussed the recent advancements related to SMN catalyst research. The various synergistic effects and interactions between different SMN catalyst components (e.g., metal nanoparticles, support material, and overcoating) make SMN catalyst research of great economic and scientific interest. This Perspective has highlighted an ALD-based overcoating ability to inhibit catalyst sintering and coking without catalytic activity loss effectively. These interactions and the nanosized nature of the metal catalyst and the overcoating pores can make these materials difficult to characterize correctly. We have also discussed how beneficial in situ and in operando characterization techniques are for understanding catalyst and overcoating evolution and stability.

Going forward, we believe systematic studies are required to fully understand how the overcoating thickness and heating conditions all affect pore formation and pore size/shape. Again, because of the changes that occur to SMN catalysts during operation, in situ and in operando characterization techniques will be vital to understanding the physical (e.g., phase changes and particle sintering) and chemical changes that occur in real-time. SAXS and XAS are powerful characterization techniques that can provide a wide range of structural and electronic information. These characterization techniques often operate at beamlines featuring synchrotron-based X-rays, offering unique and versatile experimental designs. Recently, researchers have utilized these techniques simultaneously to study change to their materials in real-time.[113−115] To the best of our knowledge, this concept has not yet been applied to studying SMN catalyst overcoating stability and pore formation. A schematic illustration of an experimental setup for simultaneous SAXS/XAS measurements can be seen in Figure 8a. In short, the incident X-ray passes through the sample and continues in the same direction while the scattered X-rays hit the detector. As the incident X-ray energy is scanned across the energy range of interest, the sample absorbs the X-rays, and X-ray fluorescence signals are generated. By placing the fluorescence detector at a 90-degree angle from the incident X-ray, we can continuously collect XAS data while also collecting SAXS images with the 2D detector. Specialized sample cells can also be utilized for such experiments to allow for controlled gas flow, temperature, pressure, and other conditions around the sample. An example of such a sample cell can be seen in Figure 8b.[116] Figure 8c,d show schematic views of the sample cell which outline the compact design of the cell. The versatility of this cell allows for many different types of in situ experiments while allowing control of both the sample atmosphere and temperature (up to ∼1270 K). These simultaneous, in situ experiments combined with specialized sample cells will be incredibly beneficial for monitoring and understanding changes to the catalyst and ALD overcoating under operational conditions.

■ ASSOCIATED CONTENT

Supporting Information

The Supporting Information is available free of charge at https://pubs.acs.org/doi/10.1021/acscatal.0c05099.

(ZIP)

https://dx.doi.org/10.1021/acscatal.0c05099
ACS Catal. 2021, 11, 2605−2619

AUTHOR INFORMATION

Corresponding Author

Tao Li − *Department of Chemistry and Biochemistry, Northern Illinois University, DeKalb, Illinois 60115, United States; X-ray Science Division, Argonne National Laboratory, Lemont, Illinois 60439, United States;* orcid.org/0000-0002-4913-4486; Email: taoli@anl.gov, tli4@niu.edu

Authors

Erik Sarnello − *Department of Chemistry and Biochemistry, Northern Illinois University, DeKalb, Illinois 60115, United States*

Zheng Lu − *Chemical Sciences and Engineering Division, Argonne National Laboratory, Lemont, Illinois 60439, United States*

Soenke Seifert − *X-ray Science Division, Argonne National Laboratory, Lemont, Illinois 60439, United States*

Randall E. Winans − *X-ray Science Division, Argonne National Laboratory, Lemont, Illinois 60439, United States;* orcid.org/0000-0002-7080-7673

Complete contact information is available at: https://pubs.acs.org/10.1021/acscatal.0c05099

Notes

The authors declare no competing financial interest.

ACKNOWLEDGMENTS

T. Li is thankful for the supported by U.S. National Science Foundation (Grant No. 1924574). This research used resources of the Advanced Photon Source, a U.S. Department of Energy (DOE) Office of Science User Facility, operated for the DOE Office of Science by Argonne National Laboratory under Contract No. DE-AC02-06CH11357.

REFERENCES

(1) Zhang, H.; Gu, X.-K.; Canlas, C.; Kropf, A. J.; Aich, P.; Greeley, J. P.; Elam, J. W.; Meyers, R. J.; Dumesic, J. A.; Stair, P. C.; Marshall, C. L. Atomic Layer Deposition Overcoating: Tuning Catalyst Selectivity for Biomass Conversion. *Angew. Chem., Int. Ed.* **2014**, *53*, 12132−12136.

(2) Lei, Y.; Lu, J.; Luo, X.; Wu, T.; Du, P.; Zhang, X.; Ren, Y.; Wen, J.; Miller, D. J.; Miller, J. T.; Sun, Y.-K.; Elam, J. W.; Amine, K. Synthesis of Porous Carbon Supported Palladium Nanoparticle Catalysts by Atomic Layer Deposition: Application for Rechargeable Lithium−O_2 Battery. *Nano Lett.* **2013**, *13*, 4182−4189.

(3) Pan, F.; Xiang, X.; Du, Z.; Sarnello, E.; Li, T.; Li, Y. Integrating photocatalysis and thermocatalysis to enable efficient CO_2 reforming of methane on Pt supported CeO_2 with Zn doping and atomic layer deposited MgO overcoating. *Appl. Catal., B* **2020**, *260*, 118189−118197.

(4) Ndolomingo, M. J.; Bingwa, N.; Meijboom, R. Review of supported metal nanoparticles: synthesis methodologies, advantages and application as catalysts. *J. Mater. Sci.* **2020**, *55*, 6195−6241.

(5) Kim, H. J.; Jackson, D. H. K.; Lee, J.; Guan, Y.; Kuech, T. F.; Huber, G. W. Enhanced Activity and Stability of TiO_2-Coated Cobalt/Carbon Catalysts for Electrochemical Water Oxidation. *ACS Catal.* **2015**, *5*, 3463−3469.

(6) Yeo, B. S.; Bell, A. T. Enhanced Activity of Gold-Supported Cobalt Oxide for the Electrochemical Evolution of Oxygen. *J. Am. Chem. Soc.* **2011**, *133*, 5587−5593.

(7) O'Neill, B. J.; Jackson, D. H. K.; Crisci, A. J.; Farberow, C. A.; Shi, F.; Alba-Rubio, A. C.; Lu, J.; Dietrich, P. J.; Gu, X.; Marshall, C. L.; Stair, P. C.; Elam, J. W.; Miller, J. T.; Ribeiro, F. H.; Voyles, P. M.; Greeley, J.; Mavrikakis, M.; Scott, S. L.; Kuech, T. F.; Dumesic, J. A. Stabilization of Copper Catalysts for Liquid-Phase Reactions by Atomic Layer Deposition. *Angew. Chem., Int. Ed.* **2013**, *52*, 13808−13812.

(8) Esswein, A. J.; McMurdo, M. J.; Ross, P. N.; Bell, A. T.; Tilley, T. D. Size-Dependent Activity of Co_3O_4 Nanoparticle Anodes for Alkaline Water Electrolysis. *J. Phys. Chem. C* **2009**, *113*, 15068−15072.

(9) Lee, J.; Jackson, D. H. K.; Li, T.; Winans, R. E.; Dumesic, J. A.; Kuech, T. F.; Huber, G. W. Enhanced stability of cobalt catalysts by atomic layer deposition for aqueous-phase reactions. *Energy Environ. Sci.* **2014**, *7*, 1657−1660.

(10) Li, S.; Gong, J. Strategies for improving the performance and stability of Ni-based catalysts for reforming reactions. *Chem. Soc. Rev.* **2014**, *43*, 7245−7256.

(11) Asami, K.; Li, X.; Fujimoto, K.; Koyama, Y.; Sakurama, A.; Kometani, N.; Yonezawa, Y. CO_2 reforming of CH_4 over ceria-supported metal catalysts. *Catal. Today* **2003**, *84*, 27−31.

(12) Iwasa, N.; Yamane, T.; Takei, M.; Ozaki, J.-i.; Arai, M. Hydrogen production by steam reforming of acetic acid: Comparison of conventional supported metal catalysts and metal-incorporated mesoporous smectite-like catalysts. *Int. J. Hydrogen Energy* **2010**, *35*, 110−117.

(13) Sitthisa, S.; Resasco, D. E. Hydrodeoxygenation of Furfural Over Supported Metal Catalysts: A Comparative Study of Cu, Pd and Ni. *Catal. Lett.* **2011**, *141*, 784−791.

(14) Deshmane, V. G.; Owen, S. L.; Abrokwah, R. Y.; Kuila, D. Mesoporous nanocrystalline TiO_2 supported metal (Cu, Co, Ni, Pd, Zn, and Sn) catalysts: Effect of metal-support interactions on steam reforming of methanol. *J. Mol. Catal. A: Chem.* **2015**, *408*, 202−213.

(15) Bartholomew, C. H. Mechanisms of catalyst deactivation. *Appl. Catal., A* **2001**, *212*, 17−60.

(16) Forzatti, P.; Lietti, L. Catalyst deactivation. *Catal. Today* **1999**, *52*, 165−181.

(17) Nkosi, B.; Coville, N. J.; Hutchings, G. J.; Adams, M. D.; Friedl, J.; Wagner, F. E. Hydrochlorination of acetylene using gold catalysts: A study of catalyst deactivation. *J. Catal.* **1991**, *128*, 366−377.

(18) Lu, J.; Liu, B.; Greeley, J. P.; Feng, Z.; Libera, J. A.; Lei, Y.; Bedzyk, M. J.; Stair, P. C.; Elam, J. W. Porous Alumina Protective Coatings on Palladium Nanoparticles by Self-Poisoned Atomic Layer Deposition. *Chem. Mater.* **2012**, *24*, 2047−2055.

(19) Barbier, J. Deactivation of reforming catalysts by coking - a review. *Appl. Catal.* **1986**, *23*, 225−243.

(20) Moulijn, J. A.; van Diepen, A. E.; Kapteijn, F. Catalyst deactivation: is it predictable?: What to do? *Appl. Catal., A* **2001**, *212*, 3−16.

(21) Arnal, P. M.; Comotti, M.; Schüth, F. High-Temperature-Stable Catalysts by Hollow Sphere Encapsulation. *Angew. Chem., Int. Ed.* **2006**, *45*, 8224−8227.

(22) Bo, Z.; Eaton, T. R.; Gallagher, J. R.; Canlas, C. P.; Miller, J. T.; Notestein, J. M. Size-Selective Synthesis and Stabilization of Small Silver Nanoparticles on TiO_2 Partially Masked by SiO_2. *Chem. Mater.* **2015**, *27*, 1269−1277.

(23) Vannice, M. A.; Wang, S. Y.; Moon, S. H. The effect of SMSI (strong metal-support interaction) behavior on CO adsorption and hydrogenation on Pd catalysts: I. IR spectra of adsorbed CO prior to and during reaction conditions. *J. Catal.* **1981**, *71*, 152−166.

(24) George, C.; Littlewood, P.; Stair, P. C. Understanding Pore Formation in ALD Alumina Overcoats. *ACS Appl. Mater. Interfaces* **2020**, *12*, 20331−20343.

(25) Alba-Rubio, A. C.; O'Neill, B. J.; Shi, F.; Akatay, C.; Canlas, C.; Li, T.; Winans, R.; Elam, J. W.; Stach, E. A.; Voyles, P. M.; Dumesic, J. A. Pore Structure and Bifunctional Catalyst Activity of Overlayers Applied by Atomic Layer Deposition on Copper Nanoparticles. *ACS Catal.* **2014**, *4*, 1554−1557.

(26) Lu, J.; Fu, B.; Kung, M. C.; Xiao, G.; Elam, J. W.; Kung, H. H.; Stair, P. C. Coking- and Sintering-Resistant Palladium Catalysts Achieved Through Atomic Layer Deposition. *Science* **2012**, *335*, 1205−1208.

(27) Doll, G. L.; Mensah, B. A.; Mohseni, H.; Scharf, T. W. Chemical Vapor Deposition and Atomic Layer Deposition of

Coatings for Mechanical Applications. *J. Therm. Spray Technol.* **2010**, *19*, 510−516.
(28) Suntola, T. Atomic layer epitaxy. *Mater. Sci. Rep.* **1989**, *4*, 261−312.
(29) Leskelä, M.; Ritala, M. Atomic Layer Epitaxy in Deposition of Various Oxide and Nitride Thin Films. *J. Phys. IV* **1995**, *5*, C5-937−C5-951.
(30) Ritala, M.; Leskelä, M.; Dekker, J.-P.; Mutsaers, C.; Soininen, P. J.; Skarp, J. Perfectly Conformal TiN and Al_2O_3 Films Deposited by Atomic Layer Deposition. *Chem. Vap. Deposition* **1999**, *5*, 7−9.
(31) George, S. M.; Ott, A. W.; Klaus, J. W. Surface Chemistry for Atomic Layer Growth. *J. Phys. Chem.* **1996**, *100*, 13121−13131.
(32) George, S. M. Atomic Layer Deposition: An Overview. *Chem. Rev.* **2010**, *110*, 111−131.
(33) Leskelä, M.; Ritala, M. Atomic Layer Deposition Chemistry: Recent Developments and Future Challenges. *Angew. Chem., Int. Ed.* **2003**, *42*, 5548−5554.
(34) Sundberg, P.; Karppinen, M. Organic and inorganic−organic thin film structures by molecular layer deposition: A review. *Beilstein J. Nanotechnol.* **2014**, *5*, 1104−1136.
(35) Lee, B. H.; Yoon, B.; Abdulagatov, A. I.; Hall, R. A.; George, S. M. Growth and Properties of Hybrid Organic-Inorganic Metalcone Films Using Molecular Layer Deposition Techniques. *Adv. Funct. Mater.* **2013**, *23*, 532−546.
(36) Longrie, D.; Deduytsche, D.; Detavernier, C. Reactor concepts for atomic layer deposition on agitated particles: A review. *J. Vac. Sci. Technol., A* **2014**, *32*, 010802−010815.
(37) Johnson, R. W.; Hultqvist, A.; Bent, S. F. A brief review of atomic layer deposition: from fundamentals to applications. *Mater. Today* **2014**, *17*, 236−246.
(38) Yan, B.; Li, X.; Bai, Z.; Song, X.; Xiong, D.; Zhao, M.; Li, D.; Lu, S. A review of atomic layer deposition providing high performance lithium sulfur batteries. *J. Power Sources* **2017**, *338*, 34−48.
(39) Zhao, Y.; Sun, X. Molecular Layer Deposition for Energy Conversion and Storage. *ACS Energy Lett.* **2018**, *3*, 899−914.
(40) Yi, H.; Du, H.; Hu, Y.; Yan, H.; Jiang, H.-L.; Lu, J. Precisely Controlled Porous Alumina Overcoating on Pd Catalyst by Atomic Layer Deposition: Enhanced Selectivity and Durability in Hydrogenation of 1,3-Butadiene. *ACS Catal.* **2015**, *5*, 2735−2739.
(41) Zhang, H.; Canlas, C.; Jeremy Kropf, A.; Elam, J. W.; Dumesic, J. A.; Marshall, C. L. Enhancing the stability of copper chromite catalysts for the selective hydrogenation of furfural with ALD overcoating (II) − Comparison between TiO_2 and Al_2O_3 overcoatings. *J. Catal.* **2015**, *326*, 172−181.
(42) Onn, T. M.; Zhang, S.; Arroyo-Ramirez, L.; Chung, Y.-C.; Graham, G. W.; Pan, X.; Gorte, R. J. Improved Thermal Stability and Methane-Oxidation Activity of Pd/Al_2O_3 Catalysts by Atomic Layer Deposition of ZrO_2. *ACS Catal.* **2015**, *5*, 5696−5701.
(43) O'Neill, B. J.; Jackson, D. H. K.; Lee, J.; Canlas, C.; Stair, P. C.; Marshall, C. L.; Elam, J. W.; Kuech, T. F.; Dumesic, J. A.; Huber, G. W. Catalyst Design with Atomic Layer Deposition. *ACS Catal.* **2015**, *5*, 1804−1825.
(44) Gould, T. D.; Izar, A.; Weimer, A. W.; Falconer, J. L.; Medlin, J. W. Stabilizing Ni Catalysts by Molecular Layer Deposition for Harsh, Dry Reforming Conditions. *ACS Catal.* **2014**, *4*, 2714−2717.
(45) O'Neill, B. J.; Miller, J. T.; Dietrich, P. J.; Sollberger, F. G.; Ribeiro, F. H.; Dumesic, J. A. Operando X-ray Absorption Spectroscopy Studies of Sintering for Supported Copper Catalysts during Liquid-phase Reaction. *ChemCatChem* **2014**, *6*, 2493−2496.
(46) Pham, H. N.; Anderson, A. E.; Johnson, R. L.; Schwartz, T. J.; O'Neill, B. J.; Duan, P.; Schmidt-Rohr, K.; Dumesic, J. A.; Datye, A. K. Carbon Overcoating of Supported Metal Catalysts for Improved Hydrothermal Stability. *ACS Catal.* **2015**, *5*, 4546−4555.
(47) Lu, J.; Liu, B.; Guisinger, N. P.; Stair, P. C.; Greeley, J. P.; Elam, J. W. First-Principles Predictions and in Situ Experimental Validation of Alumina Atomic Layer Deposition on Metal Surfaces. *Chem. Mater.* **2014**, *26*, 6752−6761.
(48) Hu, Q.; Wang, S.; Gao, Z.; Li, Y.; Zhang, Q.; Xiang, Q.; Qin, Y. The precise decoration of Pt nanoparticles with Fe oxide by atomic layer deposition for the selective hydrogenation of cinnamaldehyde. *Appl. Catal., B* **2017**, *218*, 591−599.
(49) Weng, Z.; Zaera, F. Sub-Monolayer Control of Mixed-Oxide Support Composition in Catalysts via Atomic Layer Deposition: Selective Hydrogenation of Cinnamaldehyde Promoted by (SiO_2-ALD)-Pt/Al_2O_3. *ACS Catal.* **2018**, *8*, 8513−8524.
(50) Antila, L. J.; Heikkilä, M. J.; Mäkinen, V.; Humalamäki, N.; Laitinen, M.; Linko, V.; Jalkanen, P.; Toppari, J.; Aumanen, V.; Kemell, M.; Myllyperkiö, P.; Honkala, K.; Häkkinen, H.; Leskelä, M.; Korppi-Tommola, J. E. I. ALD Grown Aluminum Oxide Submonolayers in Dye-Sensitized Solar Cells: The Effect on Interfacial Electron Transfer and Performance. *J. Phys. Chem. C* **2011**, *115*, 16720−16729.
(51) Biener, M. M.; Biener, J.; Wichmann, A.; Wittstock, A.; Baumann, T. F.; Bäumer, M.; Hamza, A. V. ALD Functionalized Nanoporous Gold: Thermal Stability, Mechanical Properties, and Catalytic Activity. *Nano Lett.* **2011**, *11*, 3085−3090.
(52) Whitney, A. V.; Elam, J. W.; Stair, P. C.; Van Duyne, R. P. Toward a Thermally Robust Operando Surface-Enhanced Raman Spectroscopy Substrate. *J. Phys. Chem. C* **2007**, *111*, 16827−16832.
(53) O'Neill, B. J.; Sener, C.; Jackson, D. H. K.; Kuech, T. F.; Dumesic, J. A. Control of Thickness and Chemical Properties of Atomic Layer Deposition Overcoats for Stabilizing Cu/γ-Al_2O_3 Catalysts. *ChemSusChem* **2014**, *7*, 3247−3251.
(54) Feng, H.; Lu, J.; Stair, P. C.; Elam, J. W. Alumina Over-coating on Pd Nanoparticle Catalysts by Atomic Layer Deposition: Enhanced Stability and Reactivity. *Catal. Lett.* **2011**, *141*, 512−517.
(55) Singh, J. A.; Yang, N.; Bent, S. F. Nanoengineering Heterogeneous Catalysts by Atomic Layer Deposition. *Annu. Rev. Chem. Biomol. Eng.* **2017**, *8*, 41−62.
(56) Lu, Z.; Piernavieja-Hermida, M.; Turner, C. H.; Wu, Z.; Lei, Y. Effects of TiO_2 in low temperature propylene epoxidation using gold catalysts. *J. Phys. Chem. C* **2018**, *122*, 1688−1698.
(57) Lu, Z.; Kizilkaya, O.; Kropf, A. J.; Piernavieja-Hermida, M.; Miller, J. T.; Kurtz, R. L.; Elam, J. W.; Lei, Y. Design and synthesis of model and practical palladium catalysts using atomic layer deposition. *Catal. Sci. Technol.* **2016**, *6*, 6845−6852.
(58) Wu, Y.; Lu, Z.; Emdadi, L.; Oh, S. C.; Wang, J.; Lei, Y.; Chen, H.; Tran, D. T.; Lee, I. C.; Liu, D. Tuning external surface of unit-cell thick pillared MFI and MWW zeolites by atomic layer deposition and its consequences on acid-catalyzed reactions. *J. Catal.* **2016**, *337*, 177−187.
(59) Puurunen, R. L. Surface chemistry of atomic layer deposition: A case study for the trimethylaluminum/water process. *J. Appl. Phys.* **2005**, *97*, 121301−12353.
(60) Puurunen, R. L.; Vandervorst, W. Island growth as a growth mode in atomic layer deposition: A phenomenological model. *J. Appl. Phys.* **2004**, *96*, 7686−7695.
(61) Schauermann, S.; Hoffmann, J.; Johánek, V.; Hartmann, J.; Libuda, J.; Freund, H.-J. Catalytic Activity and Poisoning of Specific Sites on Supported Metal Nanoparticles. *Angew. Chem., Int. Ed.* **2002**, *41*, 2532−2535.
(62) Schauermann, S.; Hoffmann, J.; Johánek, V.; Hartmann, J.; Libuda, J. Adsorption, decomposition and oxidation of methanol on alumina supported palladium particles. *Phys. Chem. Chem. Phys.* **2002**, *4*, 3909−3918.
(63) Fu, Q.; Li, W.-X.; Yao, Y.; Liu, H.; Su, H.-Y.; Ma, D.; Gu, X.-K.; Chen, L.; Wang, Z.; Zhang, H.; Wang, B.; Bao, X. Interface-Confined Ferrous Centers for Catalytic Oxidation. *Science* **2010**, *328*, 1141−1144.
(64) Cargnello, M.; Jaén, J. J. D.; Garrido, J. C. H.; Bakhmutsky, K.; Montini, T.; Gámez, J. J. C.; Gorte, R. J.; Fornasiero, P. Exceptional Activity for Methane Combustion over Modular $Pd@CeO_2$ Subunits on Functionalized Al_2O_3. *Science* **2012**, *337*, 713−717.
(65) Wang, C.; Wang, H.; Yao, Q.; Yan, H.; Li, J.; Lu, J. Precisely Applying TiO_2 Overcoat on Supported Au Catalysts Using Atomic Layer Deposition for Understanding the Reaction Mechanism and Improved Activity in CO Oxidation. *J. Phys. Chem. C* **2016**, *120*, 478−486.

https://dx.doi.org/10.1021/acscatal.0c05099
ACS Catal. 2021, 11, 2605−2619

(66) Yao, Q.; Wang, C.; Wang, H.; Yan, H.; Lu, J. Revisiting the Au Particle Size Effect on TiO_2-Coated Au/TiO_2 Catalysts in CO Oxidation Reaction. *J. Phys. Chem. C* **2016**, *120*, 9174−9183.
(67) Cao, L.; Lu, J. Atomic-scale engineering of metal−oxide interfaces for advanced catalysis using atomic layer deposition. *Catal. Sci. Technol.* **2020**, *10*, 2695−2710.
(68) Wen, Y.; Cai, J.; Zhang, J.; Yang, J.; Shi, L.; Cao, K.; Chen, R.; Shan, B. Edge-Selective Growth of MCp_2 (M = Fe, Co, and Ni) Precursors on Pt Nanoparticles in Atomic Layer Deposition: A Combined Theoretical and Experimental Study. *Chem. Mater.* **2019**, *31*, 101−111.
(69) Lu, Z.; Tracy, R. W.; Abrams, M. L.; Nicholls, N. L.; Barger, P. T.; Li, T.; Stair, P. C.; Dameron, A. A.; Nicholas, C. P.; Marshall, C. L. Atomic Layer Deposition Overcoating Improves Catalyst Selectivity and Longevity in Propane Dehydrogenation. *ACS Catal.* **2020**, *10*, 13957−13967.
(70) Liu, D.; Zemlyanov, D.; Wu, T.; Lobo-Lapidus, R. J.; Dumesic, J. A.; Miller, J. T.; Marshall, C. L. Deactivation mechanistic studies of copper chromite catalyst for selective hydrogenation of 2-furfuraldehyde. *J. Catal.* **2013**, *299*, 336−345.
(71) Gong, Y.; Palacio, D.; Song, X.; Patel, R. L.; Liang, X.; Zhao, X.; Goodenough, J. B.; Huang, K. Stabilizing Nanostructured Solid Oxide Fuel Cell Cathode with Atomic Layer Deposition. *Nano Lett.* **2013**, *13*, 4340−4345.
(72) Lei, Y.; Lee, S.; Low, K.-B.; Marshall, C. L.; Elam, J. W. Combining electronic and geometric effects of ZnO-promoted Pt nanocatalysts for aqueous phase reforming of 1-propanol. *ACS Catal.* **2016**, *6*, 3457−3460.
(73) Adair, K. R.; Zhao, C.; Banis, M. N.; Zhao, Y.; Li, R.; Cai, M.; Sun, X. Highly Stable Lithium Metal Anode Interface via Molecular Layer Deposition Zircone Coatings for Long Life Next-Generation Battery Systems. *Angew. Chem., Int. Ed.* **2019**, *58*, 15797−15802.
(74) Kint, J.; Mattelaer, F.; Vandenbroucke, S. S. T.; Muriqi, A.; Minjauw, M. M.; Nisula, M.; Vereecken, P. M.; Nolan, M.; Dendooven, J.; Detavernier, C. Molecular Layer Deposition of "Magnesicone", a Magnesium-based Hybrid Material. *Chem. Mater.* **2020**, *32*, 4451−4466.
(75) Van de Kerckhove, K.; Mattelaer, F.; Deduytsche, D.; Vereecken, P. M.; Dendooven, J.; Detavernier, C. Molecular layer deposition of "titanicone", a titanium-based hybrid material, as an electrode for lithium-ion batteries. *Dalton Trans.* **2016**, *45*, 1176−1184.
(76) Abdulagatov, A. I.; Ashurbekova, K. N.; Ashurbekova, K. N.; Amashaev, R. R.; Rabadanov, M. K.; Abdulagatov, I. M. Molecular Layer Deposition and Thermal Transformations of Titanium-(Aluminum)-Vanadium Hybrid Organic-Inorganic Films. *Russ. J. Appl. Chem.* **2018**, *91*, 347−359.
(77) Meng, X. An overview of molecular layer deposition for organic and organic−inorganic hybrid materials: mechanisms, growth characteristics, and promising applications. *J. Mater. Chem. A* **2017**, *5*, 18326−18378.
(78) Liang, X.; Yu, M.; Li, J.; Jiang, Y.-B.; Weimer, A. W. Ultra-thin microporous−mesoporous metal oxide films prepared by molecular layer deposition (MLD). *Chem. Commun.* **2009**, *46*, 7140−7142.
(79) Ingale, P.; Guan, C.; Kraehnert, R.; Naumann d'Alnoncourt, R.; Thomas, A.; Rosowski, F. Design of an active and stable catalyst for dry reforming of methane via molecular layer deposition. *Catal. Today* **2021**, *362*, 47−54.
(80) Molina Piper, D.; Lee, Y.; Son, S.-B.; Evans, T.; Lin, F.; Nordlund, D.; Xiao, X.; George, S. M.; Lee, S.-H.; Ban, C. Cross-linked aluminum dioxybenzene coating for stabilization of silicon electrodes. *Nano Energy* **2016**, *22*, 202−210.
(81) Min, B. K.; Wallace, W. T.; Goodman, D. W. Synthesis of a Sinter-Resistant, Mixed-Oxide Support for Au Nanoclusters. *J. Phys. Chem. B* **2004**, *108*, 14609−14615.
(82) Ma, Z.; Brown, S.; Howe, J. Y.; Overbury, S. H.; Dai, S. Surface Modification of Au/TiO_2 Catalysts by SiO_2 via Atomic Layer Deposition. *J. Phys. Chem. C* **2008**, *112*, 9448−9457.
(83) Ray, N. A.; Van Duyne, R. P.; Stair, P. C. Synthesis Strategy for Protected Metal Nanoparticles. *J. Phys. Chem. C* **2012**, *116*, 7748−7756.
(84) Liu, X.; Zhu, Q.; Lang, Y.; Cao, K.; Chu, S.; Shan, B.; Chen, R. Oxide-Nanotrap-Anchored Platinum Nanoparticles with High Activity and Sintering Resistance by Area-Selective Atomic Layer Deposition. *Angew. Chem., Int. Ed.* **2017**, *56*, 1648−1652.
(85) Lu, J.; Stair, P. C. Low-Temperature ABC-Type Atomic Layer Deposition: Synthesis of Highly Uniform Ultrafine Supported Metal Nanoparticles. *Angew. Chem., Int. Ed.* **2010**, *49*, 2547−2551.
(86) Piernavieja-Hermida, M.; Lu, Z.; White, A.; Low, K.-B.; Wu, T.; Elam, J. W.; Wu, Z.; Lei, Y. Towards ALD thin film stabilized single-atom Pd_1 catalysts. *Nanoscale* **2016**, *8*, 15348−15356.
(87) Karwal, S.; Li, T.; Yanguas-Gil, A.; Canlas, C. P.; Lei, Y.; Mane, A. U.; Libera, J. A.; Seifert, S.; Winans, R. E.; Elam, J. W. Tailoring nanopore formation in atomic layer deposited ultrathin films. *J. Vac. Sci. Technol., A* **2018**, *36*, 01A103−7.
(88) Tauster, S. J. Strong metal-support interactions. *Acc. Chem. Res.* **1987**, *20*, 389−394.
(89) Hayek, K.; Kramer, R.; Paál, Z. Metal-support boundary sites in catalysis. *Appl. Catal., A* **1997**, *162*, 1−15.
(90) Fu, Q.; Wagner, T. Interaction of nanostructured metal overlayers with oxide surfaces. *Surf. Sci. Rep.* **2007**, *62*, 431−498.
(91) Lu, Z.; Liu, X.; Zhang, B.; Gan, Z.; Tang, S.; Ma, L.; Wu, T.; Nelson, G. J.; Qin, Y.; Turner, C. H.; Lei, Y. Structure and reactivity of single site Ti catalysts for propylene epoxidation. *J. Catal.* **2019**, *377*, 419−428.
(92) Salami, H.; Poissant, A.; Adomaitis, R. A. Anomalously high alumina atomic layer deposition growth per cycle during trimethylaluminum under-dosing conditions. *J. Vac. Sci. Technol., A* **2017**, *35*, 01B101.
(93) Manandhar, K.; Wollmershauser, J. A.; Boercker, J. E.; Feigelson, B. N. Growth per cycle of alumina atomic layer deposition on nano- and micro-powders. *J. Vac. Sci. Technol., A* **2016**, *34*, 021519−9.
(94) Zhang, J.; Lu, Z.; Wu, W.; Tran, D. T.; Shang, W.; Chen, H.; Lei, Y.; Li, Z.; Wang, M.; Woehl, T. J.; Liu, D. Mesopore differences between pillared lamellar MFI and MWW zeolites probed by atomic layer deposition of titania and consequences on photocatalysis. *Microporous Mesoporous Mater.* **2019**, *276*, 260−269.
(95) Coile, M. W.; Young, M. J.; Libera, J. A.; Mane, A. U.; Elam, J. W. High-capacity rotary drum for atomic layer deposition onto powders and small mechanical parts in a hot-walled viscous flow reactor. *J. Vac. Sci. Technol. A* **2020**, *38*, 052403.
(96) Scheffe, J. R.; Francés, A.; King, D. M.; Liang, X.; Branch, B. A.; Cavanagh, A. S.; George, S. M.; Weimer, A. W. Atomic layer deposition of iron (III) oxide on zirconia nanoparticles in a fluidized bed reactor using ferrocene and oxygen. *Thin Solid Films* **2009**, *517*, 1874−1879.
(97) Solano, E.; Dendooven, J.; Feng, J.-Y.; Brüner, P.; Minjauw, M. M.; Ramachandran, R. K.; Van Daele, M.; Van de Kerckhove, K.; Dobbelaere, T.; Coati, A.; Hermida-Merino, D.; Detavernier, C. In situ study of the thermal stability of supported Pt nanoparticles and their stabilization via atomic layer deposition overcoating. *Nanoscale* **2020**, *12*, 11684−11693.
(98) Levine, J. R.; Cohen, J. B.; Chung, Y. W.; Georgopoulos, P. Grazing-incidence small-angle X-ray scattering: new tool for studying thin film growth. *J. Appl. Crystallogr.* **1989**, *22*, 528−532.
(99) Molina, L. M.; Lee, S.; Sell, K.; Barcaro, G.; Fortunelli, A.; Lee, B.; Seifert, S.; Winans, R. E.; Elam, J. W.; Pellin, M. J.; Barke, I.; von Oeynhausen, V.; Lei, Y.; Meyer, R. J.; Alonso, J. A.; Fraile Rodríguez, A.; Kleibert, A.; Giorgio, S.; Henry, C. R.; Meiwes-Broer, K.-H.; Vajda, S. Size-dependent selectivity and activity of silver nanoclusters in the partial oxidation of propylene to propylene oxide and acrolein: A joint experimental and theoretical study. *Catal. Today* **2011**, *160*, 116−130.
(100) Li, T.; Karwal, S.; Aoun, B.; Zhao, H.; Ren, Y.; Canlas, C. P.; Elam, J. W.; Winans, R. E. Exploring Pore Formation of Atomic

https://dx.doi.org/10.1021/acscatal.0c05099
ACS Catal. 2021, 11, 2605−2619

Layer-Deposited Overlayers by in Situ Small- and Wide-Angle X-ray Scattering. *Chem. Mater.* **2016**, *28*, 7082−7087.
(101) Levin, I.; Brandon, D. Metastable Alumina Polymorphs: Crystal Structures and Transition Sequences. *J. Am. Ceram. Soc.* **1998**, *81*, 1995−2012.
(102) Groen, J. C.; Peffer, L. A. A.; Pérez-Ramirez, J. Pore size determination in modified micro- and mesoporous materials. Pitfalls and limitations in gas adsorption data analysis. *Microporous Mesoporous Mater.* **2003**, *60*, 1−17.
(103) Sayers, D. E.; Stern, E. A.; Lytle, F. W. New Technique for Investigating Noncrystalline Structures: Fourier Analysis of the Extended X-Ray—Absorption Fine Structure. *Phys. Rev. Lett.* **1971**, *27*, 1204−1207.
(104) Yano, J.; Yachandra, V. K. X-ray absorption spectroscopy. *Photosynth. Res.* **2009**, *102*, 241−254.
(105) Shen, X.; Dai, S.; Zhang, S.; Lu, Z.; Zhang, C.; Graham, G. W.; Lei, Y.; Pan, X.; Peng, Z. Oxidation-Induced Atom Diffusion and Surface Restructuring in Faceted Ternary Pt−Cu−Ni Nanoparticles. *Chem. Mater.* **2019**, *31*, 1720−1728.
(106) Peng, C.; Ran, N.; Wan, G.; Zhao, W.; Kuang, Z.; Lu, Z.; Sun, C.; Liu, J.; Wang, L.; Chen, H. Engineering Active Fe Sites on Nickel−Iron Layered Double Hydroxide through Component Segregation for Oxygen Evolution Reaction. *ChemSusChem* **2020**, *13*, 811−818.
(107) Pan, F.; Li, B.; Sarnello, E.; Fei, Y.; Gang, Y.; Xiang, X.; Du, Z.; Zhang, P.; Wang, G.; Nguyen, H. T.; Li, T.; Hu, Y. H.; Zhou, H.-C.; Li, Y. Atomically Dispersed Iron−Nitrogen Sites on Hierarchically Mesoporous Carbon Nanotube and Graphene Nanoribbon Networks for CO_2 Reduction. *ACS Nano* **2020**, *14*, 5506−5516.
(108) Li, J.-C.; Maurya, S.; Kim, Y. S.; Li, T.; Wang, L.; Shi, Q.; Liu, D.; Feng, S.; Lin, Y.; Shao, M. Stabilizing Single-Atom Iron Electrocatalysts for Oxygen Reduction via Ceria Confining and Trapping. *ACS Catal.* **2020**, *10*, 2452−2458.
(109) Cao, S.; Chan, T.-S.; Lu, Y.-R.; Shi, X.; Fu, B.; Wu, Z.; Li, H.; Liu, K.; Alzuabi, S.; Cheng, P.; Liu, M.; Li, T.; Chen, X.; Piao, L. Photocatalytic pure water splitting with high efficiency and value by Pt/porous brookite TiO_2 nanoflutes. *Nano Energy* **2020**, *67*, 104287.
(110) Pan, F.; Li, B.; Sarnello, E.; Fei, Y.; Feng, X.; Gang, Y.; Xiang, X.; Fang, L.; Li, T.; Hu, Y. H.; Wang, G.; Li, Y. Pore-Edge Tailoring of Single-Atom Iron−Nitrogen Sites on Graphene for Enhanced CO_2 Reduction. *ACS Catal.* **2020**, *10*, 10803−10811.
(111) Yang, W.; Lu, Z.; Vogler, B.; Wu, T.; Lei, Y. Enhancement of Copper Catalyst Stability for Catalytic Ozonation in Water Treatment Using ALD Overcoating. *ACS Appl. Mater. Interfaces* **2018**, *10*, 43323−43326.
(112) Cao, L.; Liu, W.; Luo, Q.; Yin, R.; Wang, B.; Weissenrieder, J.; Soldemo, M.; Yan, H.; Lin, Y.; Sun, Z.; Ma, C.; Zhang, W.; Chen, S.; Wang, H.; Guan, Q.; Yao, T.; Wei, S.; Yang, J.; Lu, J. Atomically dispersed iron hydroxide anchored on Pt for preferential oxidation of CO in H_2. *Nature* **2019**, *565*, 631−635.
(113) Povia, M.; Herranz, J.; Binninger, T.; Nachtegaal, M.; Diaz, A.; Kohlbrecher, J.; Abbott, D. F.; Kim, B.-J.; Schmidt, T. J. Combining SAXS and XAS To Study the Operando Degradation of Carbon-Supported Pt-Nanoparticle Fuel Cell Catalysts. *ACS Catal.* **2018**, *8*, 7000−7015.
(114) Groppo, E.; Lazzarini, A.; Carosso, M.; Bugaev, A.; Manzoli, M.; Pellegrini, R.; Lamberti, C.; Banerjee, D.; Longo, A. Dynamic Behavior of Pd/P4VP Catalyst during the Aerobic Oxidation of 2-Propanol: A Simultaneous SAXS/XAS/MS Operando Study. *ACS Catal.* **2018**, *8*, 6870−6881.
(115) Cormary, B.; Li, T.; Liakakos, N.; Peres, L.; Fazzini, P.-F.; Blon, T.; Respaud, M.; Kropf, A. J.; Chaudret, B.; Miller, J. T.; Mader, E. A.; Soulantica, K. Concerted Growth and Ordering of Cobalt Nanorod Arrays as Revealed by Tandem in Situ SAXS-XAS Studies. *J. Am. Chem. Soc.* **2016**, *138*, 8422−8431.
(116) Chupas, P. J.; Chapman, K. W.; Kurtz, C.; Hanson, J. C.; Lee, P. L.; Grey, C. P. A versatile sample-environment cell for non-ambient X-ray scattering experiments. *J. Appl. Crystallogr.* **2008**, *41*, 822−824.

https://dx.doi.org/10.1021/acscatal.0c05099
ACS Catal. 2021, 11, 2605−2619